Journal of Structural Geology 199 (2025) 105461

Contents lists available at ScienceDirect

Journal of Structural Geology

journal homepage: www.elsevier.com/locate/sg

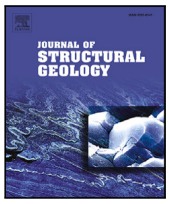

Mid-crustal strain localisation triggered by localised fluid influx and activation of dissolution–precipitation creep

Manon Carpenter *, Sandra Piazolo, Tim Craig, Tim J. Wright

COMET, Institute of Geophysics and Tectonics, School of Earth and Environment, University of Leeds, Leeds, UK

ARTICLE INFO

Keywords:
Strain localisation
Dissolution–precipitation creep
Mid-crust rheology
Fluid-rock interaction

ABSTRACT

Understanding mid-crustal deformation is vital for determining the spatial and temporal distribution of strain localisation, with implications for upper-crust deformation including seismic hazard. Here, we conduct fieldwork and microstructural and minerochemical analyses on the amphibolite-facies, 100-m-wide Upper Badcall shear zone in northwest Scotland, which deforms initially anhydrous quartzofeldspathic gneiss and a mafic dyke. We show that with increasing strain, m-scale strain distribution and mineral chemistry become increasingly homogeneous, while hydrous phases and syntectonic quartz veins become more abundant. With increasing strain there is an overall increase in grain size, grain boundary alignment and shape preferred orientation in amphibole, plagioclase and quartz. Only amphibole and large grained quartz exhibit crystallographic preferred orientation in strained areas. Subtle microstructures that may be overlooked elsewhere, particularly in felsic gneiss, indicate dominant activity of dissolution–precipitation creep and equivalent rheological weakening in both mafic and felsic rocks. We propose that brittle fractures, now preserved as syntectonic quartz veins, allowed localised fluid-infiltration in previously anhydrous crust. This triggered local retrogressive reactions and introduced sufficient grain boundary fluid for deformation to favour dissolution–precipitation creep over dislocation creep. Our study suggests that dissolution–precipitation creep may be more dominant in mid- to lower-crustal localised zones of deformation than previously thought.

1. Introduction

The majority of displacement accumulated in the mid- to lower-continental crust is accommodated in shear zones, the ductile counterparts of brittle faults in crustal-scale structures, where strain is higher than in the surrounding wall rock (Sorensen, 1983; Henstock et al., 1997; Yamasaki et al., 2014; Clerc et al., 2015; Fagereng et al., 2024). Identifying the mechanisms that govern strain localisation is essential for understanding the occurrence and distribution of significant crustal deformation and related hazards, such as earthquakes. To localise strain in discrete zones requires a localised weakening mechanism. Such a weakening process is likely to be the result of a dynamic combination of factors, depending on the geological setting and involving an interplay between ductile and brittle deformation (e.g. Rutter and Brodie, 1985; Bürgmann and Dresen, 2008; Brander et al., 2012; Corvò et al., 2021).

We know the rheology of deforming mid- to lower-continental crust is predominantly viscous, based on observations of exhumed mm- to km-scale shear zones (Ramsay and Graham, 1970; Carreras and Casas, 1987; Carreras, 2001; Svahnberg and Piazolo, 2010; Gerbi et al., 2016) and geophysical observations (Kaufmann and Amelung, 2000; Kenner and Segall, 2003; Bürgmann and Dresen, 2008; Weiss et al., 2019). Experiments have long been used to determine the governing flow laws that describe the mechanisms of viscous deformation observed in these regions (e.g. Rybacki and Dresen, 2000; Hirth and Kohlstedt, 2003). However, two overarching questions remain, namely (1) what controls the localisation of strain into discrete zones in specific areas and (2) which deformation mechanisms are dominant in these localised, discrete zones. If we know the dominant deformation mechanisms active in these zones, it is possible to predict and/or reconstruct the form of the appropriate flow law by which the rocks deform (e.g. linear-viscous versus power-law). With appropriate flow laws we can build geophysical models that enable us to interpret geodetic data, in which observations of active fault zones provide short-term snapshots of time-varying deformation (e.g. Hussain et al., 2018; Takeuchi and Fialko, 2012; Yamasaki et al., 2014).

Previous studies have put forward a number of candidate models to explain how strain localises in shear zones (for review see Fossen and Cavalcante, 2017, and references therein). For example, deformation dominated by dislocation creep follows a power-law flow law in which strain localisation is inherent, due to a stress exponent that is generally between 3–5 (Schmid et al., 1980; Boland and Tullis, 1986;

* Corresponding author.
E-mail address: eemrca@leeds.ac.uk (M. Carpenter).

https://doi.org/10.1016/j.jsg.2025.105461
Received 3 January 2025; Received in revised form 18 April 2025; Accepted 14 May 2025
Available online 1 June 2025

Carter et al., 1993; Karato and Wu, 1993). Localised weakening may occur if associated dynamic recrystallisation weakens rock through grain size reduction, which subsequently drives a switch to grain-size-sensitive deformation mechanisms where grain size is small (e.g. Kirby, 1985; Drury, 2005; Warren and Hirth, 2006; Svahnberg and Piazolo, 2010). Shear zones may also initiate due to rock heterogeneity at macro or micro scale (Handy, 1994; Dell'Angelo and Tullis, 1996; Ingles et al., 1999; Mandal et al., 2004), including fractures or joints and dykes (Segall and Simpson, 1986; Pennacchioni and Mancktelow, 2007; Smith et al., 2015), or rheological contrasts between different lithologies (e.g. Corvò et al., 2022). Extrinsic factors can play a role, for example, if fluid introduction weakens rock through hydrous metamorphic reactions that lead to softening through mineral assemblage change (Teall, 1885; Ramsay and Graham, 1970; Beach, 1980; Rutter and Brodie, 1985; Moore et al., 2020; Bras et al., 2021), and/or reaction-driven grain size reduction (Kirby, 1985; Stünitz and Tullis, 2001; Smith et al., 2015; Soret et al., 2019; Stenvall et al., 2019; Mansard et al., 2020). It is changes in both extrinsic and intrinsic parameters, such as temperature, fluid availability, stress, and grain size, that can drive a switch in the mechanism that dominates deformation (e.g. Kirby, 1985; Rutter and Brodie, 1988; Viegas et al., 2016). Therefore, the dominance of different deformation mechanisms may continuously change as the deformation history develops, and specific rheological behaviour may be transient (Rutter et al., 2001; Steffen et al., 2001; Gardner et al., 2017a; Bras et al., 2021, and references therein). Such transient rheological behaviour of the crust is reflected in geophysical observations of active faults, with increasingly long observation periods now showing a range of transient processes in the mid- to lower-crust following larger earthquakes (e.g. Weiss et al., 2019; Tian et al., 2020).

The dominant deformation mechanism active in the mid-crust is commonly thought to be dislocation creep (Bürgmann and Dresen, 2008, and references therein). This is based on observations of quartz- and feldspar-rich natural shear zones (e.g. Kruse and Stünitz, 1999; Stipp et al., 2002; Piazolo and Passchier, 2002; Czaplińska et al., 2015; Lusk and Platt, 2020; Orlandini and Mahan, 2020) and experiments (e.g. Hirth and Tullis, 1994). The microstructural signatures of dislocation creep include bent crystal lattices within individual grains, seen optically as undulose extinction, the formation of subgrains, grain size reduction by subgrain rotation (dynamic recrystallisation), crystallographic preferred orientation (CPO), heterogeneous nucleation and core-mantle structures (Trimby et al., 1998; Prior et al., 2002; Piazolo et al., 2002; Passchier and Trouw, 2005; Halfpenny et al., 2006). Because dislocation creep can be active at medium to high stresses and temperatures, without the need for fluids, it has historically been considered the dominant deformation mechanism in the mid- to lower-crust where fluids are thought to be scarce (Rutter, 1976; Gratier et al., 2013; Gomez-Rivas et al., 2020). Consequently, estimates of the strength of Earth's crust are generally based on dislocation creep-deformed grain size pietzometry (Twiss, 1977; Cross and Skemer, 2019; Goddard et al., 2020; Tokle and Hirth, 2021; Platt et al., 2015).

An alternative deformation mechanism, which requires the presence of fluids, is dissolution–precipitation creep (aka pressure solution), which is a major mechanism of ductile deformation in the upper-crust (Gratier, 1987; Wheeler, 1992; Gratier et al., 2013; Putnis, 2021). Reported signatures of dissolution–precipitation creep include truncation of grains and zoning, embayed/indented grain boundaries and preferentially formed, asymmetric rims, overgrowths, tails, or beards in the pressure shadows of large grains, which may be chemically distinct (Knipe, 1989; Wintsch and Yi, 2002; Stokes et al., 2012; Gratier et al., 2013; Wassmann and Stöckhert, 2013). In addition, coeval metamorphic reactions may occur which lead to phase changes during deformation (Stünitz et al., 2020; Malvoisin and Baumgartner, 2021; Lee et al., 2022). In contrast to common reports of dissolution–precipitation creep in the upper-crust (e.g. pressure solution creep, Gratier et al. 2013), studies that interpret deformation in the mid- to lower-crust to be dominated by this mechanism are historically scarce. However, in recent years, an increasing number of studies have identified the role of dissolution–precipitation creep in the mid- to lower-crust, and include studies of cm- to m-scale shear zones (Menegon et al., 2008; Lee et al., 2022; Moore et al., 2020, 2024; Mérit et al., 2025), km-scale shear zones (Trepmann and Seybold, 2019; Wintsch et al., 2024), and deformed km-scale units (amphibolite, Díaz Aspiroz et al. 2007, Stokes et al. 2012, Giuntoli et al. 2018; granodioritic gneiss, Wintsch and Yi 2002). Yet to be widely documented is the role of dissolution–precipitation creep in large-scale mid- to lower-crustal shear zones, and the process by which strain localises in these specific zones. Whether the scarcity in recognition of this processes is a true reflection of its limited occurrence, or rather a lack of widespread recognition of this process, remains unclear. It is important that we understand the significance of dissolution–precipitation creep as a deformation mechanism in Earth's crust, to ensure that, in building geophysical models to understand the occurrence and distribution of significant crustal deformation, we can best characterise the material properties and processes that govern such deformation.

To address this gap in our knowledge, and assess by what process dissolution–precipitation creep may be a viable mechanism for strain localisation in the mid-crust, we investigate in detail the 100-m-wide, amphibolite-facies Upper Badcall shear zone in NW Scotland which deforms originally dry Archean granulite-facies rocks cross-cut by a mafic dyke (Beach et al. 1974, Coward and Potts 1983 and references therein; Tatham and Casey 2007; Fig. 1). This shear zone is ideally suited for our study as it is well constrained in terms of accumulated strain, and its exceptional exposure allows for detailed strain mapping and sampling. We use field, microstructural and minerochemical observations and analyses to show that this shear zone deformed predominantly by dissolution–precipitation creep. We interpret that the necessary availability of grain boundary fluid was enabled by fluid infiltration, through localised brittle fractures, into previously dry, dislocation creep-deformed rock. Hydration does not only trigger localised, retrogressive metamorphic reactions, but allows deformation to favour dissolution–precipitation creep over dislocation creep where sufficient fluid is present.

2. Geological setting and sample locations: Upper Badcall shear zone in the Lewisian Gneiss Complex

The Upper Badcall shear zone is situated within the Archean Assynt terrane, which comprises part of the Central Region of the Lewisian Gneiss Complex (LGC), northwest Scotland (Fig. 1; Peach 1907, Sutton and Watson 1950, Friend and Kinny 2001, Kinny et al. 2005). Granulite-facies, pyroxene-bearing quartzofeldspathic gneisses formed during an early, 'Badcallian' event (previously known as 'Scourian' granulites), c. 2800–2700 Ma at conditions between 750-990 °C and 7–11 kbar (Sutton and Watson, 1950; Park, 1970; Chapman and Moorbath, 1977; Hamilton et al., 1979; Cartwright and Barnicoat, 1987; Sills and Rollinson, 1987; Goodenough et al., 2013). This gneiss was deformed and retrogressed to hornblende- and biotite gneisses at amphibolite-facies conditions during either, or both, the 'Inverian' amphibolite-facies event (Evans 1965, c. 2490–2480 Ma, Friend and Kinny 1995), or the 'Laxfordian' amphibolite-facies event (c. 1750 Ma, Moorbath et al. 1969; Kinny and Friend 1997). At 2400–1900 Ma a suite of mafic, predominantly dolerite, dykes (the Scourie dyke swarm) intruded under conditions of 450–500 °C and 5–7 kbar (Sutton and Watson, 1950; Tarney, 1963; Park and Tarney, 1987; Cohen et al., 1991). Deformation related to the 'Laxfordian' event is identified where amphibolite-facies structures truncate the Scourie dykes.

The shear zone at Upper Badcall is part of a population of 'Laxfordian', amphibolite-facies shear zones observed across the Assynt terrane, which deform both the gneisses and Scourie dykes (Fig. 1a). These include 1–100 m wide discrete, steeply dipping shear zones (Beach et al., 1974; Goodenough et al., 2010) and km-wide structures (Laxford,

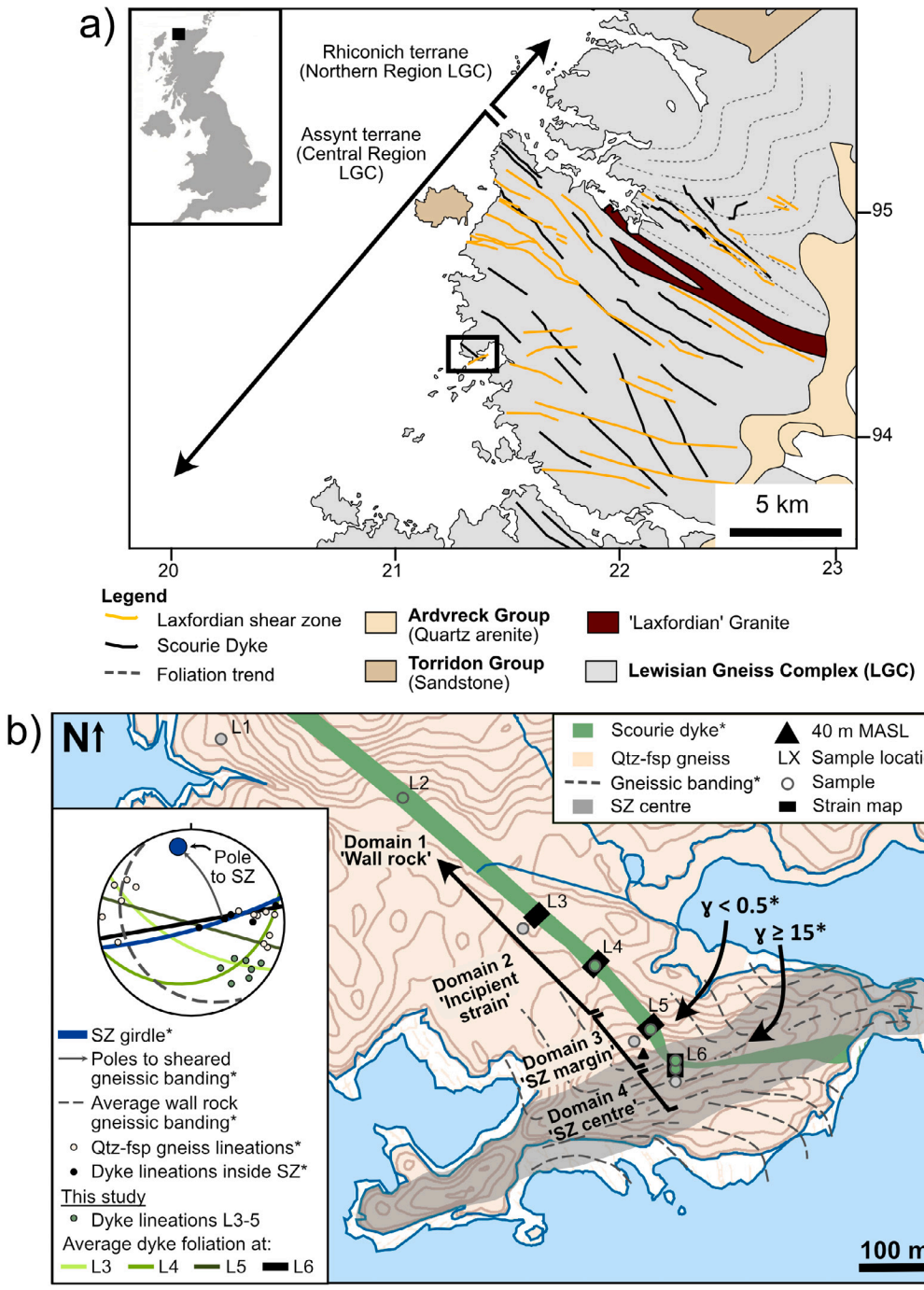

Fig. 1. The geological setting of the field area in NW Scotland, UK; (a) Overview geological map of the Central Region of the Lewisian Gneiss Complex (LGC), modified after Beach (1974b), Beach et al. (1974) and Goodenough et al. (2010). Black box shows the location of the field area, and the co-ordinate system is British National Grid. Inset: Overview map of the UK. (b) Field area in Upper Badcall, showing the mafic Scourie dyke and surrounding quartzofeldspathic gneiss deformed into the shear zone. The asterisk (*) denotes data, mapping and results from Tatham and Casey (2007). MASL: Meters Above Sea Level. (For interpretation of the references to colour in this figure legend, the reader is referred to the web version of this article.)

aka Tarbet, Shear Zone, Beach et al. 1974, Goodenough et al. 2010; and Canisp, aka Stoer, Shear Zone, Attfield 1987). Beach (1974b) estimates a total of 22.5 km of horizontal displacement across these shear zones. This 'Laxfordian' tectonometamorphism occurred at mid-crustal amphibolite-facies conditions estimated at 510–660 °C and 5–8 kbar in the Assynt terrane (Beach, 1973; Cartwright, 1990; Pearce and Wheeler, 2014).

The Upper Badcall shear zone is approximately 100 m wide, trending ENE-WSW with subvertical foliation formed at a high angle to the gneissic foliation in the wall rock (Fig. 1b; Coward and Potts 1983, Tatham and Casey 2007). The shear zone deforms both the quartzofeldspathic gneiss wall rock and a ~ 10-m-wide, near vertical mafic Scourie dyke, in a ductile zone of oblique left-lateral strike slip which offsets the dyke by c. 190 m (Tatham and Casey, 2007). In the same study the authors calculate a shear strain by simple shear of at least 15 at the shear zone centre, based on the deflection of fabric in the surrounding gneisses. We present results from both the gneiss and dyke, which we sampled at varying distances along a general transect from 500 m from the shear zone centre, where 'Laxfordian' deformation is minimal, to the shear zone centre itself. Our samples represent the

variation in strain along this transect (Fig. 1; Table S1 in Supplementary materials).

3. Methods

3.1. Thin section preparation and optical analysis

Samples were cut perpendicular to foliation (XY) and parallel to the lineation (X), where present, and polished to ~ 30 μm thickness. Thin sections were first evaluated using a petrographic optical microscope. We obtained overview thin section scans using plustek OpticFilm 8100 scanner at 7200 resolution and photomicrographs using GX-CAM HiChrome-HR4 camera and GX Capture imaging software. For quantitative orientation and qualitative mineral chemistry analyses, respectively using electron backscatter diffraction (EBSD) and energy dispersive spectroscopy (EDX), samples were polished for a further 9 min using a colloidal silica-water solution. Samples were coated with a 5 nm and 10 nm thick carbon coat for EBSD analysis, and backscattered electron (BSE), cathodoluminesence (CL) imaging, and electron microprobe analysis (EMPA), respectively.

3.2. Electron microscope based techniques

3.2.1. Cathodoluminescence imaging

CL imaging of quartz microstructures was carried out using a Tescan VEGA3 XM at Leeds Electron Microscopy and Spectroscopy Centre (LEMAS, University of Leeds, UK). The imaging was performed at high-vacuum conditions with an accelerating voltage of 20 kV and a working distance of 15 mm.

3.2.2. Quantitative crystallographic orientation analysis with qualitative mineral chemistry

Simultaneous crystallographic orientation (EBSD) and qualitative mineral chemistry (EDX) data were collected on a regular grid using a FEI Quanta 650 SEM at LEMAS equipped with the CMOS Symmetry EBSD detector, and X-Max 80 mm^2 EDX detector using AZtec software, all from Oxford Instruments. Analyses were performed at high-vacuum conditions with an accelerating voltage of 30 kV, a working distance of around 25 mm on a specimen tilted by 70°. Data was acquired on a regular grid. Large area maps (3 μm step size) were obtained for each sample, and small area, higher spatial resolution maps (1.5 μm step size) were obtained to observe finer features. The data were then processed using AZtecCrystal software (Oxford Instruments; see Supplementary material for details).

To determine the shape orientation of grains we plot the fitted ellipse angle for the three main phases in both the dyke and gneiss (plagioclase, amphibole and quartz), with the X-axis in maps oriented 90–270°, and Z-axis oriented 0–180°, normal to foliation. We assess the internal deformation of grains using cumulative disorientation profiles across individual grains, including subgrains where relevant, and grain relative orientation deviation (GROD) maps where for each grain the mean orientation is calculated and a colour scheme is used to show the deviation of each analysis points' crystallographic orientation relative to the mean crystallographic orientation.

We present grain size (equivalent circle diameter) as both standard and area-weighted fraction. In both the gneiss and dyke wall rock, the large grains are so few by number that they do not alter the standard grain size results significantly; however, area-weighted fraction grain size histogram shows 2 distinct populations present in at least the wall rocks. To highlight these populations, we separate the main phase grain populations into small and large grain subsets, determined using area-weighted fraction grain size graphs. In the dyke small grains for each phase are: amphibole > 200 μm, plagioclase > 300 μm and quartz > 100 μm equivalent circle diameter (plus all clinopyroxene which are max 90 μm). In the gneiss small grains for each phase are plagioclase < 200 μm, quartz < 100 μm and amphibole < 120 μm equivalent circle diameter. So-called large grains are those above these values.

3.2.3. Mineral abundance estimates

We estimate mineral abundance using AZtecCrystal large area phase maps, plus AZtecCrystal EDX maps to estimate minerals that did not index well or at all (e.g. chlorite, biotite and muscovite). Estimates from phase maps and EDX have been cross-checked with overall mineral proportions present in thin section scale. Abbreviated mineral names follow the database from Whitney and Evans (2010), unless stated otherwise.

3.2.4. EDX data processing: Relative chemistry difference in plagioclase

To obtain relative and spatial chemistry difference between plagioclase compositions present in the gneiss and dyke we reconstructed EDX spectra for 1–3 mm^2 areas using TrueMap in AZtec, and obtained element abundance by stoichiometry combined with oxygen, normalised and reported as oxide%. Analysis data is available in Supplementary materials Table S2. We report plagioclase compositions as relative weight fractions:

$$\#\mathrm{Ab}\ \text{or}\ \#\mathrm{An} = \frac{X\mathrm{Ab}\ \text{or}\ X\mathrm{An}}{X\mathrm{Ab} + X\mathrm{An}} \tag{1}$$

Where

$$X\mathrm{Ab} = \frac{\mathrm{Na_2O\ wt\%}}{\mathrm{MW\ of\ Na_2O}} \times \frac{\text{Molar proportion of } \mathrm{Na_2O} \text{ in albite}}{100} \tag{2}$$

And

$$X\mathrm{An} = \frac{\mathrm{CaO\ wt\%}}{\mathrm{MW\ of\ CaO}} \times \frac{\text{Molar proportion of CaO in anorthite}}{100} \tag{3}$$

3.2.5. Electron microprobe analysis

Quantitative chemical point analyses were obtained using a Jeol 8230 microprobe at LEMAS, with a 15–20 kV accelerating voltage, 10 nA beam current and a 1–5 μm spot size. The instrument was calibrated using standards WRS1485 amphibole and Kakanuii Hornblende for amphibole, and SPH1, SKL1 and SKBy1 for plagioclase analysis. Analysis data is available in Supplementary materials Tables S3 and S4. Areas of large amphibole grains containing ilmenite inclusions, and areas of plagioclase grains which are pock-marked sericite, were avoided. Where clear surfaces survived in the clay-altered plagioclase, intergrowth light and dark inclusions on 1–5 μm scale exist. These could not be avoided and resulted in a mixed signal and scattered data points. These points we disregarded in our analyses.

4. Results

4.1. General field relationships and outcrop characteristics

The mafic, now metamorphosed to amphibolite, dyke forms a low ridge that strikes NW/SE to the NW of the shear zone, and the quartzofeldspathic gneiss outcrops as patches amongst low vegetation (Fig. 2a i). The shear zone coincides with a topographic high that reaches 40 m elevation above the surrounding coastline (Figs. 1b; 2a ii). Lineations within the dyke are object lineations (Piazolo and Passchier, 2002), including both amphibole grain and plagioclase aggregate lineations. Lineations rotate from plunging ~ 20-40° SE outside the shear zone to plunging ~ 20-40° E in the shear zone centre (Fig. 1b). In general there is an increase in the number of small and discontinuous (0.5–20 mm wide, up to 60 cm long) quartz veins in the dyke with increasing proximity to the shear zone centre. The veins are parallel to subparallel to the fabric and exhibit a range of geometries from planar to isoclinally folded (axial plane parallel to deformation fabric).

Over 500 m NW from the shear zone centre the now amphibolite dyke is undeformed with a meta-igneous isotropic fabric defined by black amphibole and white plagioclase in 1–10 mm clusters (L2, Figs. 1b; 2b i; see Section 4.4 and Table 1 for detailed phase abundance). The quartzofeldspathic gneiss (L1) exhibits a weakly banded fabric dominated by lighter bands, comprised of equant 1–3 mm plagioclase and quartz grains, interspersed with darker amphibole-rich bands (Fig.

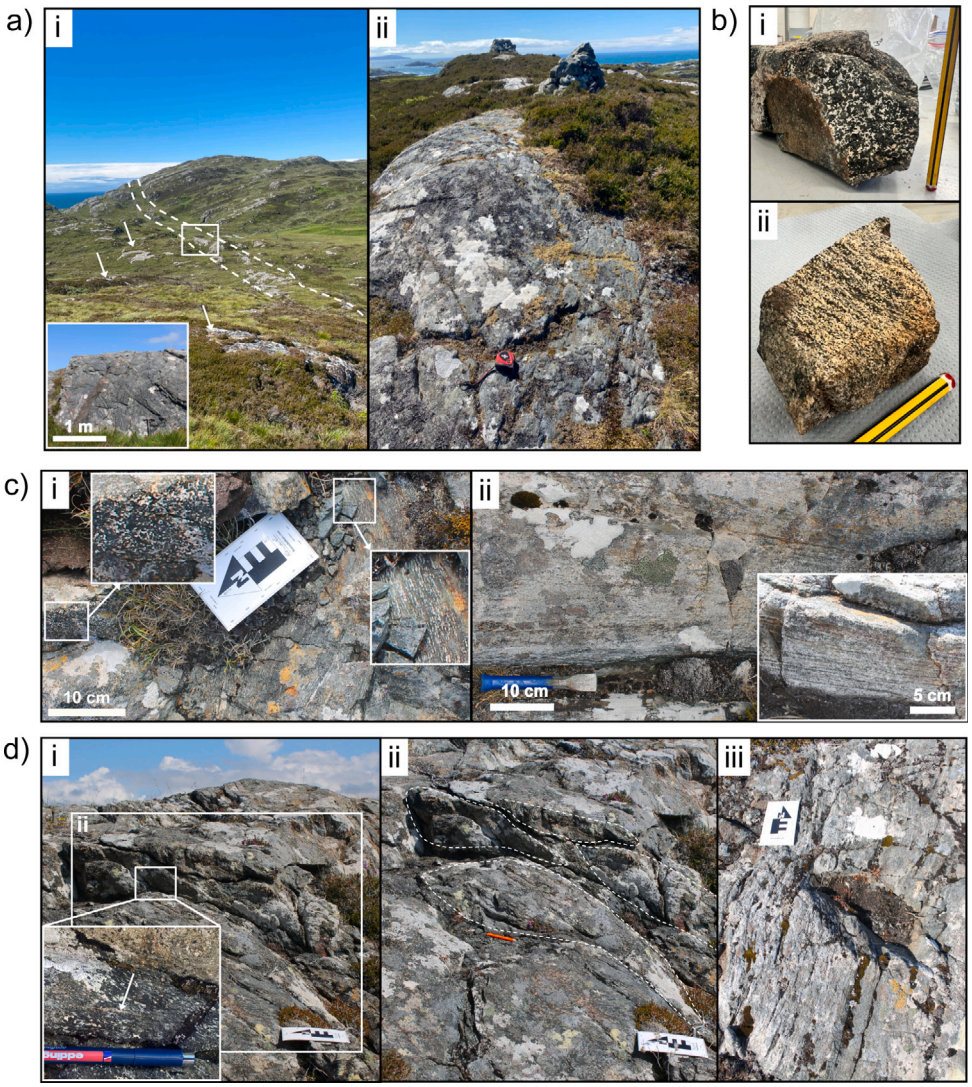

Fig. 2. Photos showing an overview of the field area and outcrop or hand samples from >200 m from shear zone centre. (a) (i) Looking NW over field area from shear zone centre, dashed lines trace dyke outcrop and white arrows indicate gneiss outcrop. Inset: dyke outcrop 350 m NW of shear zone (L3). (ii) Looking W from shear zone centre. (b) Samples collected over 500 m from shear zone centre of (i) dyke (L2) and (ii) gneiss (L1), note cm-wide light and dark bands. (c) 350 m NW of shear zone centre (L3) showing (i) dyke shape fabric variation and (ii) gneiss. (d) 250 m NW of shear zone centre (L4) (i) lenses of relatively undeformed dyke enveloped by anastomosing deformed dyke. Inset: singular quartz vein in band of low strain fabric. (ii) annotated version and schematic illustration of (d) (i), and (iii) gneiss.

2b ii; see Section 4.4 and Table 1 for detailed phase abundance). Between 350 m (L3) and 250 m (L4) NW of the shear zone centre, elongate lenses of undeformed dyke are enveloped by anastomosing bands of deformed dyke which exhibits a shape fabric, defined by aligned, elongate plagioclase clusters, that varies in strength over a cm- to m-scale, perpendicular to fabric strike (Figs. 1b; 2c i & d i–ii). Rarely, singular, mm wide quartz veins are present, subparallel to the deformation fabric (Fig. 2d i inset). The gneiss has a stronger fabric here, defined by a few mm-cm wide alternating light (plagioclase and quartz) and dark (amphibole) bands, and contains distinct discontinuous bands of quartz a few cm long (Fig. 2c ii & d iii).

Approximately 100 m NW from the shear zone centre (L5) more than 50% of the dyke is deformed and the shape fabric is dominantly planar, steeply dipping (290/80° NE) and continuous on a m-scale perpendicular to strike, rather than anastomosing around undeformed lenses (Fig. 3a i). Within the deformed areas of the dyke multiple subparallel quartz veins are observed, ~ 1–2 mm wide and up to 60 cm long (Fig. 3a ii). The gneiss has a strong planar fabric defined by light mm-cm wide plagioclase and quartz bands, and less frequent dark mm-wide amphibole bands (Fig. 3a iii).

In the shear zone centre the dyke is entirely deformed and both the dyke and gneiss have a pervasive, planar, steeply dipping (80-90°) fabric which strikes E/W and a lineation that plunges 20-40° E. The dyke-gneiss contact is also planar, concordant with the gneiss and dyke fabric, and shows no rheological contrast features such as boudinage or pinch and swell structures (Fig. 3b i). The gneiss is weathered grey, similar to outside the shear zone, but is more creamy white to light brown on a fresh surface and foliation is defined by mm-scale bands of quartz and plagioclase (Fig. 3b i inset). Aligned elongate plagioclase clusters again define the deformed dyke fabric, the elongation of which varies in intensity on 10's cm- to m-scale, perpendicular to strike (Fig. 3b ii). Multiple fabric-subparallel quartz veins up to 2 cm wide are present within the deformed dyke, some of which exhibit isoclinal folds with axial surfaces subparallel to the fabric (Fig. 3b iii-iv).

4.2. Quantification of field shape fabric variation and quartz vein abundance in the dyke

Four strain maps, conducted along 10–15 m long transects perpendicular to the dyke, show a significant change in strain type and distribution at the outcrop scale, and quartz vein abundance, from ~

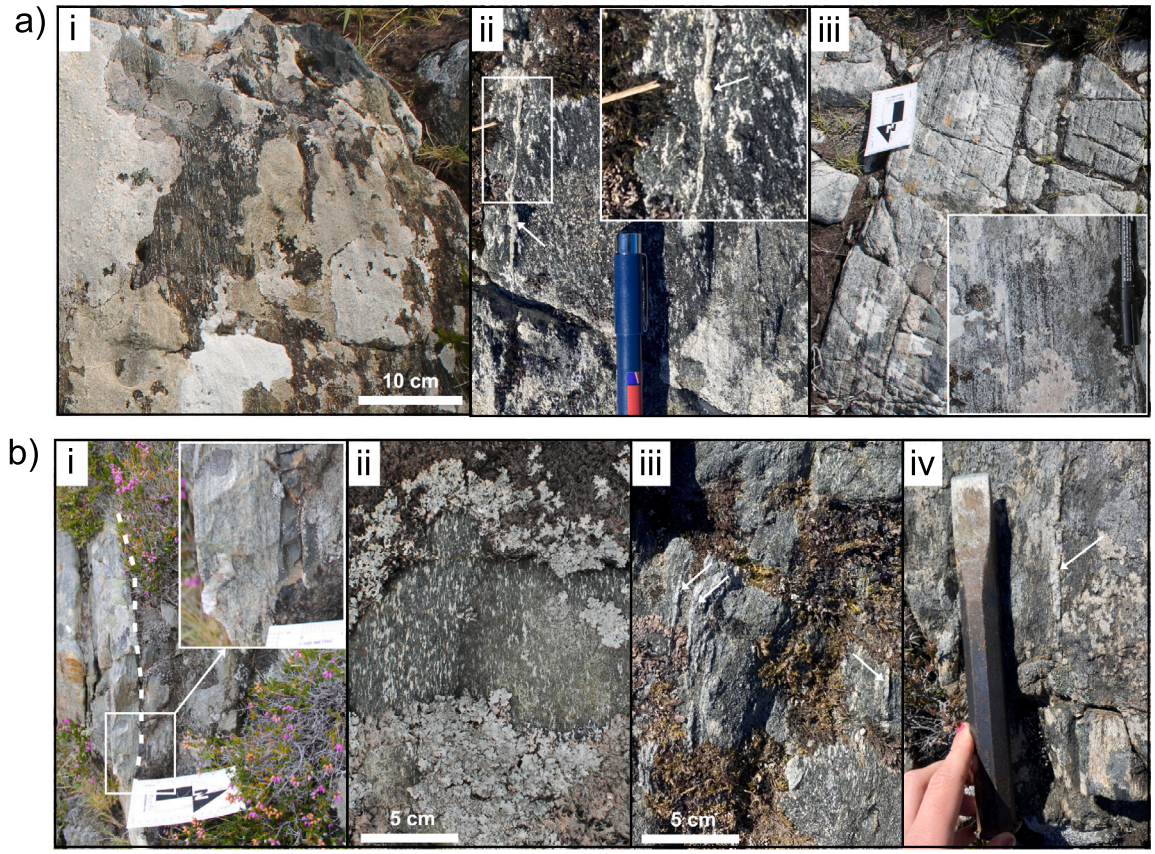

Fig. 3. Photos of outcrops within 100 m of shear zone centre. (a) 100 m NW of shear zone centre; (i) dyke looking SE; note high degree of planar shear related foliation, (ii) dyke, looking down, white arrows highlight quartz veins, (iii) gneiss, note dominance of light areas and mm sized dark bands. (b) Shear zone centre; (i) subvertical, planar dyke-gneiss contact (white dashed line) with dyke on right and gneiss on left; looking W. (ii) Dyke, looking down, with vertical foliation and (iii) & (iv) abundance of variably sheared quartz veins in the dyke (white arrows).

350 m away from the shear zone, to the shear zone centre (L3-6, Figs. 1b; 4). To quantify these changes we defined four strain types (T) based on the shape fabric of plagioclase aggregates identified in the field: (T0) background isotropic igneous texture with no preferred shape orientation, (T1) shape preferred orientation but no defined foliation, (T2) elongated plagioclase aggregates define ≥ 1 mm spaced foliation fabric and, (T3) <1 mm spaced foliation fabric (Fig. 4a).

At 350 m from the shear zone centre (L3) the fabric in the dyke is dominated by (60%) T0 lenses which are embedded in anastomosing, relatively narrow cm – 10's cm wide bands of predominantly T1 fabric. No quartz veins are observed. At 250 m from the shear zone centre (L4) the width of T1 bands is increased to ~ 50 cm and the geometry is more planar. One foliation-parallel quartz vein is observed within a T1 band between undeformed T0 lenses (Fig. 2d i inset). 100 m from the shear zone centre (L5), 70% of the strain map has T1 fabric, which is generally planar except for where it wraps around a couple of undeformed lenses. Across this transect 13 quartz veins are observed, 1–2 mm wide and up to 60 cm long. In the shear zone centre (L6) 100% of the dyke exhibits T1 or higher planar fabric and 20 quartz veins, up to 2 cm wide and subparallel to fabric, are observed within the strain map.

Overall, the percentage of deformed rock volume, and intensity of shape fabric, increases from 30% deformed rock 350 m and 250 m from the shear zone centre, to 100% deformed rock in the shear zone centre (Fig. 4c). In the two strain maps furthest from the shear zone centre, T1 bands anastomose around undeformed lenses of T0 dyke, whereas closer to the shear zone the fabric becomes planar and more homogeneous (Fig. 4d). The abundance of quartz veins (fabric-parallel or subparallel, 0.5–20 mm wide and up to 60 cm long) increases towards the shear zone (Fig. 4 b & c).

4.3. Structural domains

Based on the field strain fabric mapping and shear strain (γ) derived by Tatham and Casey (2007), we distinguish 4 structural domains to determine the change in structure and chemistry towards the shear zone (Figs. 1b; 4d). Domain 1 'wall rock' represents the background rock where minimal deformation associated with the shear zone has occurred. Domain 2 'incipient strain' represents incipient shear, where localised bands of strain anastomose around undeformed lenses of rock. In Domain 3 'shear zone margin' ≥ 70% of the rock is deformed and fabric is predominantly planar, oblique to the shear zone (γ <0.5 according to Tatham and Casey 2007). In Domain 4 'shear zone centre' 100% of the rock is deformed, and lineations and planar fabric are parallel to the shear zone ($\gamma \sim \geq 15$).

4.4. Microstructures and phase distribution and abundance

Here we present an overview of the microstructures, phase distribution and mineral chemistry observed in the dominant fabric type (dyke type T0-3; gneiss weak to strong) for the respective structural domain (Fig. 1b). Table S1 in Supplementary materials lists the samples used for analyses.

4.4.1. Domain 1 'wall rock'. Undeformed dyke and high grade foliated granulitic gneiss; dominant dyke fabric type T0

Dyke: The wall rock consists of 60% amphibole, 30% plagioclase, 5% quartz and 1% clinopyroxene, clinozoisite, titanite, ilmenite and apatite (Table 1). The texture is isotropic and correlates with T0 (Section 4.2; Fig. 5a i). 1–3 mm clusters of either amphibole or plagioclase grains dominate, within which different grain populations are

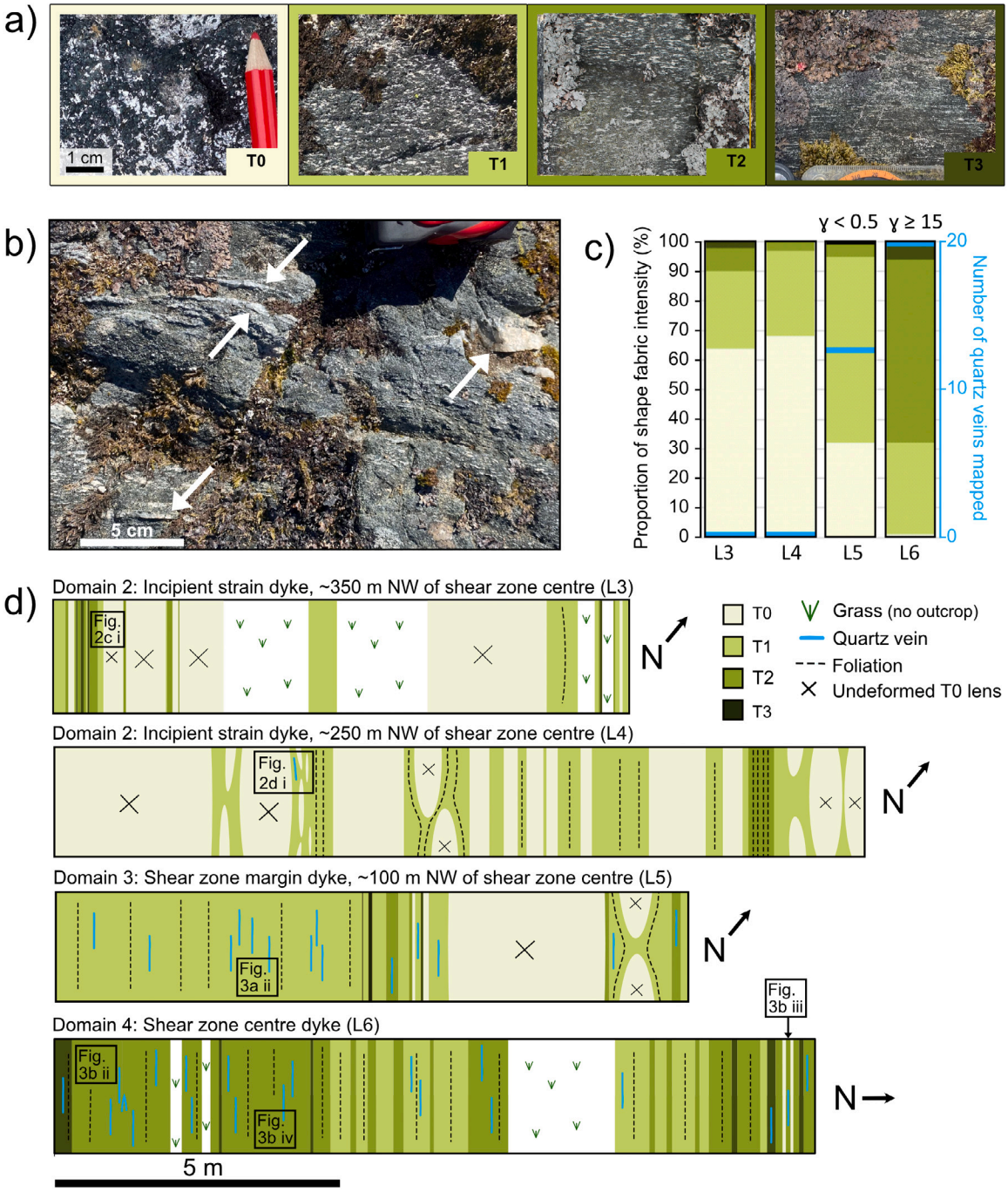

Fig. 4. Field photos and maps, showing the field characterisation of dyke shape fabric types (T0-3) in structural domains 2–4. (a) Typical outcrop images of strain types (T) in dyke based on field shape fabric; note *T* number increases with increasing strain. (b) White arrows highlight cm-scale quartz veins in shear zone centre dyke T2. (c) Field shape fabric intensity and quartz vein abundance for each strain map shown in (d), with strain estimates from Tatham and Casey (2007). 'T' colours correspond to (a) where light to dark green corresponds to no/low to high shape fabric. (d) Representation of measured strain maps along 10–15 m transects across dyke with decreasing distance to shear zone. See Fig. 1b for locations (L3-6). (For interpretation of the references to colour in this figure legend, the reader is referred to the web version of this article.)

observed, determined by their grain size and mineralogy (Fig. 5a i-iv). The plagioclase clusters consist of 60% large (~ 0.3–0.8 mm) and 40% small (<0.3 mm) grains. Of the large plagioclase grains, ~ 70% appear light brown in colour due to extensive alteration to sericite and ~ 30% are colourless and minimally altered. The small plagioclase grains are generally colourless, minimally altered and exist between and at the margins of large plagioclase grains (Fig. 5a ii-iv). Individual, large (~ 0.2–0.5 mm) amphibole grains form roughly 10 area% and exhibit a range of chemistry: (1) opaque ilmenite-speckled cores with rims which are replaced to varying degrees by clear green amphibole, (2) entirely clear green amphibole or (3) clear green amphibole with quartz ± clinopyroxene inclusions (Fig. 5a ii-iv). Distinct areas of small (<0.1 mm) intermixed amphibole and quartz, sometimes with remnant <0.1 mm clinopyroxene in their centre, comprise 50 area% (Fig. 5a ii-iv). At the boundary of plagioclase clusters and grains, a margin of medium size (0.1–0.2 mm) amphibole often exists, effectively separating plagioclase from amphibole-quartz ± clinopyroxene areas (Fig. 5a iv). Individual large (0.1–0.2 mm) quartz grains are spatially associated with large plagioclase and amphibole (Fig. 5a iv), all of which exhibit undulose extinction to some extent.

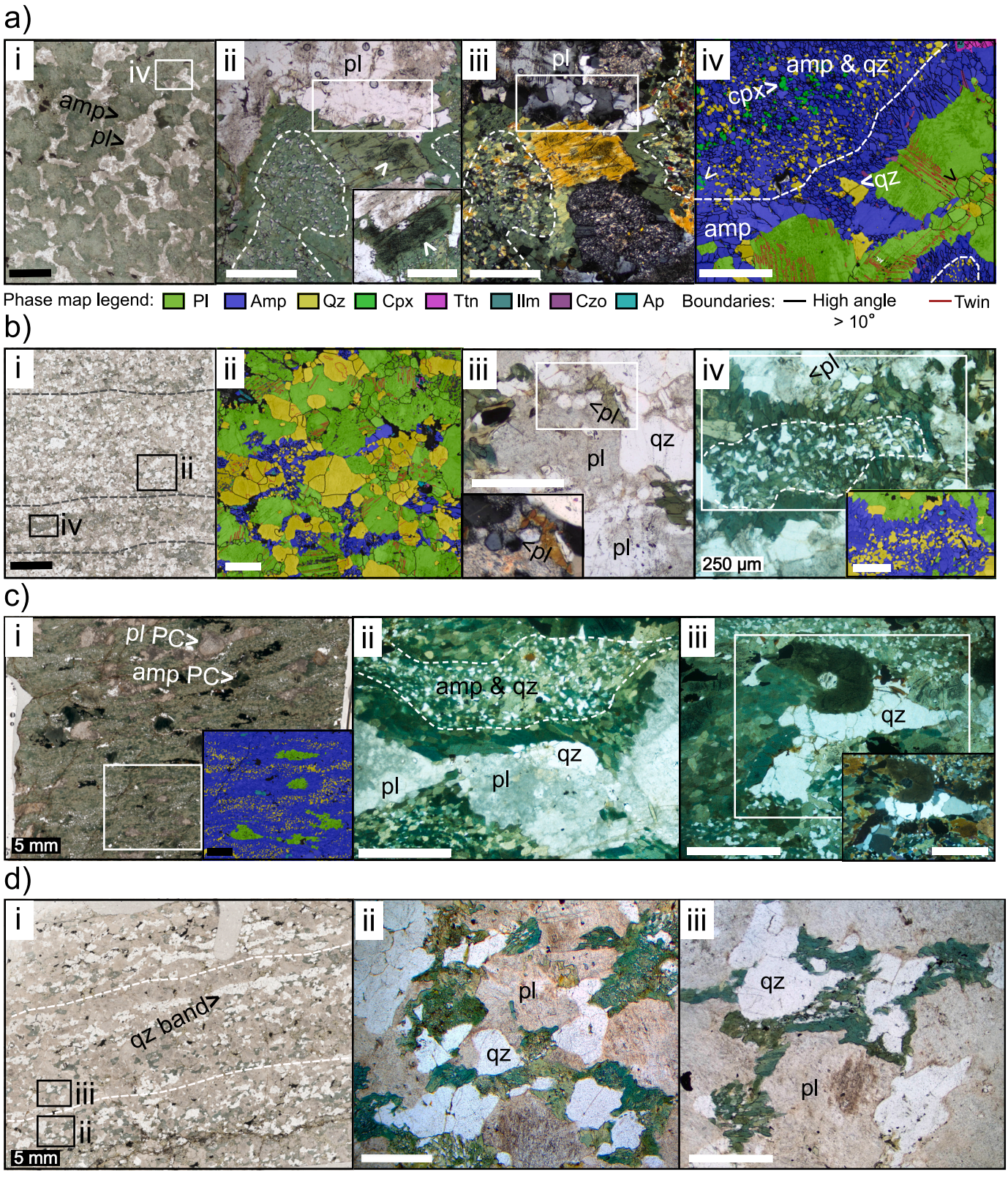

Fig. 5. Optical microstructures of domain 1 'wall rock' and 2 'incipient strain' dyke (a & c) and gneiss (b & d), shown with thin section scans, photomicrographs in plane-polarised light (PPL) or cross-polarised light (XPL) where indicated, and EBSD false colour phase maps. Phase abbreviations after Whitney and Evans (2010). (a) Dyke, domain 1 T0 (AS2239); (i) isotropic fabric, (ii) amp cores with replacement front (white arrows) and amp-qz areas outlined with dashed line, (iii) XPL version of (ii) showing unaltered small pl grains (white boxes), and (iv) outline of parent cpx grains (dashed lines). (b) Gneiss, domain 1 (AS2240a); (i) weak fabric (dashed lines), (ii) phase distribution, (iii) unaltered small pl grains, and (iv) amp-qz areas (dashed lines) surrounded by medium amp. (c) Dyke, domain 2 T1 (AS2153); (i) & (ii) elongate fabric and amp-qz areas (dashed line) surrounded by medium amp, and (iii) qz beard in pressure shadow with XPL inset. (d) Gneiss, domain 2 (AS2151); (i) weak fabric (dashed lines) with discontinuous qz band (black arrow) and (ii) & (iii) phase distribution. Black scale bar: 1 mm and white bar: 500 µm, unless stated otherwise. (For interpretation of the references to colour in this figure legend, the reader is referred to the web version of this article.)

Table 1
Mineral proportion estimates from EBSD phase maps, EDX maps and thin sections. Domain numbers refer to domains: (1) wall rock, (2) incipient shear, (3) shear zone margin and (4) shear zone centre (see Fig. 1b). Mineral abbreviations after Whitney and Evans (2010). Hydrous phases are listed in blue, late alteration phases are listed in orange. See Fig. 8 for the change in amphibole and plagioclase composition with microstructure and domain.

Dyke sample	Domain	Fabric type	Amp	Pl	Qz	Cpx	Czo	Ilm	Ttn	Ap	Chl	Ms
AS2239	1	T0	60	30	5	1	1	1	1	0	0	0
AS2153	2	T1	70	20	10	0	<1	1	<1	0	0	0
AS2237*	3	T1	70	20	10							
AS2160	4	T2	75	15	10	0	<1	1	0	<1	0	0
AS2158	4	T3	80	5	10	0	5	1	0	<1	0	0
*no EBSD data												
Gneiss sample	**Domain**	**Strain**	**Pl**	**Qtz**	**Amp**	**Bt**	**Czo**	**Ilm**	**Ttn**	**Ap**	**Chl**	**Ms**
AS2240A	1	Low	55	30	10	0	<1	<1	<1	<1	5	0
AS2151	2	Low	55	30	10	0	<1	<1	<1	<1	5	0
AS2155	3	Medium	60	30	5	5	1	<1	0	<1	<1	<1
AS2157	4	High	60	30	3	5	<1	0	0	0	2	<1

Gneiss: The gneiss wall rock consists of 55% plagioclase, 30% quartz, 10% amphibole, 5% chlorite and ≤ 1% ilmenite, clinozoisite, titanite and apatite (Table 1). It has a weak fabric defined by lighter quartz-plagioclase bands and darker green amphibole-rich bands (Fig. 5b i). Large plagioclase (0.2–1 mm), quartz (0.1–0.6 mm) and amphibole grains (0.1–0.4 mm) form roughly 60 area% (Fig. 5b ii). Of the large plagioclase, around 70% are light brown where altered to sericite and 30% are colourless and minimally altered (Fig. 5b iii). Small (<0.2 mm), unaltered plagioclase grains exist between or at the boundaries of larger plagioclase grains and make up 10 area% (Fig. 5b iii). Approximately 30 area% consists of distinct domains of smaller (<0.1 mm) intermixed amphibole-quartz, with a margin of medium sized amphibole grains where adjacent to plagioclase (Fig. 5b iv). Similar to in the dyke the large plagioclase, quartz and amphibole exhibit minor undulose extinction.

4.4.2. Domain 2 'incipient strain'. Low strain fabrics; dominant deformation dyke fabric type T0

Dyke: Here 65%–70% of the dyke has no (T0) strain fabric and 30% is comprised of low (T1) strain fabric (Fig. 4). Compared to domain 1 T0, T1 strain fabric has increased amphibole and quartz (10% and 5% more respectively), 10% less plagioclase and no clinopyroxene. It has a similar phase distribution to the dyke wall rock, however, grains and grain domains are now elongated to form a weak fabric and here large grains (amphibole and plagioclase) are evenly distributed throughout the smaller-grained matrix as porphyroclasts (Fig. 5c i-ii). Plagioclase clusters, now comprised predominantly of small grains, show the beginnings of attenuation and disaggregation in the X direction. Amphibole grains which envelop plagioclase clusters are rotated to align in the X direction (Fig. 5c ii). Large grained quartz crystallises in asymmetric pressure shadows around plagioclase and amphibole porphyroclasts, forming beards of quartz grown preferentially in the X direction (Fig. 5c iii).

Gneiss: The gneiss mineralogy, grain populations and phase distribution are similar to the 'wall rock' domain 1, however here the fabric is more strongly defined by narrow, discontinuous quartz or amphibole bands within wider, continuous plagioclase bands (Fig. 5d i). Similar to domain 1 dyke, amphibole grains adjacent to plagioclase are rotated to align in the X direction, and an overall shape preferred orientation is observed (Fig. 5d ii–iii).

4.4.3. Domain 3 'shear zone margin'. Heterogeneously deformed dyke and quartzofeldspathic gneiss; dominant dyke fabric type T1

Dyke: The dyke is composed of 65% T1 strain fabric and 30% T0 (Fig. 4). While domain 2 and domain 3 T1 strain fabric appear similar in outcrop and share the same mineralogy, in the microstructure the phase distribution differs. Here, small-grained amphibole-quartz bands are not observed and instead intermediate grain size (0.1–0.3 mm) amphibole forms the matrix framework (Fig. 6a i). This amphibole is elongate and strongly aligned in the X direction (amp_e, Fig. 6a ii). A small number (~ 5%) of amphibole grains are more equant, almost rounded and are oriented differently to amp_e (amp_r, Fig. 6a ii). In addition, a number of ilmenite-speckled amphibole porphyroclasts remain, with a rim of clear amphibole grown preferentially in the X direction (Fig. 6a iii). Small (<0.1 mm) quartz is predominantly observed as individual grains around the tails of elongated plagioclase clusters, and as disaggregated bands within amphibole matrix (Fig. 6a i). These individual quartz, and occasionally plagioclase, grains are often elongate with preferentially grown tails formed in the X direction, or exist as individual grains with high aspect ratios between elongate amphibole grains (Fig. 6a ii). These grains are often seen to 'indent' amphibole grains (Fig. 6a ii).

Gneiss: Compared to domains 1 and 2 gneiss, domain 3 gneiss comprises 5% more plagioclase and 5% less of both amphibole and chlorite (Table 1). Notably, 5% biotite is observed, spatially associated with amphibole, and plagioclase is generally unaltered with only <5% altered to sericite (Fig. 6b i-ii). The large plagioclase and large individual quartz grains observed in domains 1 and 2 gneiss are not present here; instead small (0.2 mm) plagioclase dominates the matrix, interspersed with individual grains or discontinuous bands of 0.1 mm quartz ± amphibole and biotite, aligned in the X direction (Fig. 6b iii). Occasional quartz bands, boudinaged and semi-continuous in the X-direction (Fig. 6b iii), have a larger (~ 0.5 mm) grain size compared to the matrix and exhibit undulose extinction.

4.4.4. Domain 4 'shear zone centre'. Strongly and homogeneously deformed dyke, strongly deformed gneiss; main deformation dyke fabric T2

Dyke: Here the dyke is composed predominantly of T2 (60%) and T1 (30%) strain fabric and some T3 (7%, Fig. 4). Compared to T1, T2 dyke consists of 5% more amphibole, 5% less plagioclase and titanite is not present as an accessory mineral (Table 1). Grain populations and distribution is very similar to domain 3 T1, except that plagioclase clusters are elongated here into discontinuous bands rather than clusters, with a grain size of 0.1–0.5 mm (Fig. 6c i). 40% of the plagioclase is altered to sericite, with both altered and unaltered plagioclase intermixed within the plagioclase bands and individual grains (Fig. 6c ii). Similar to domain 3, T1, intermediate (0.5 mm), elongate and aligned amp_e forms the matrix framework (Fig. 6c i–ii). Amp_e often align to form continuous linked surfaces extending several grains in the X direction, with or without small <0.15 mm individual quartz or plagioclase grains grown between aligned amp_e (Fig. 6c iii). As in domain 3 T1, these small quartz and plagioclase are observed as disseminated bands in the amphibole matrix and at the margins of plagioclase clusters or amphibole porphyroclasts, as thin films between amp_e or elongate with tails preferentially grown in the X direction (Fig. 6c iv–vi). In quartz these preferentially grown tails exhibit reduced CL-response compared to the overall grain (Fig. 6c v). Quartz, plagioclase and amphibole grains themselves often 'indent' adjacent amphibole grains in the Z direction, perpendicular to foliation (Fig. 6c iv & vi).

T3 mineralogy and phase distribution is distinct from T1-2; only 5% plagioclase remains and 5% clinozoisite is present, quartz, plagioclase,

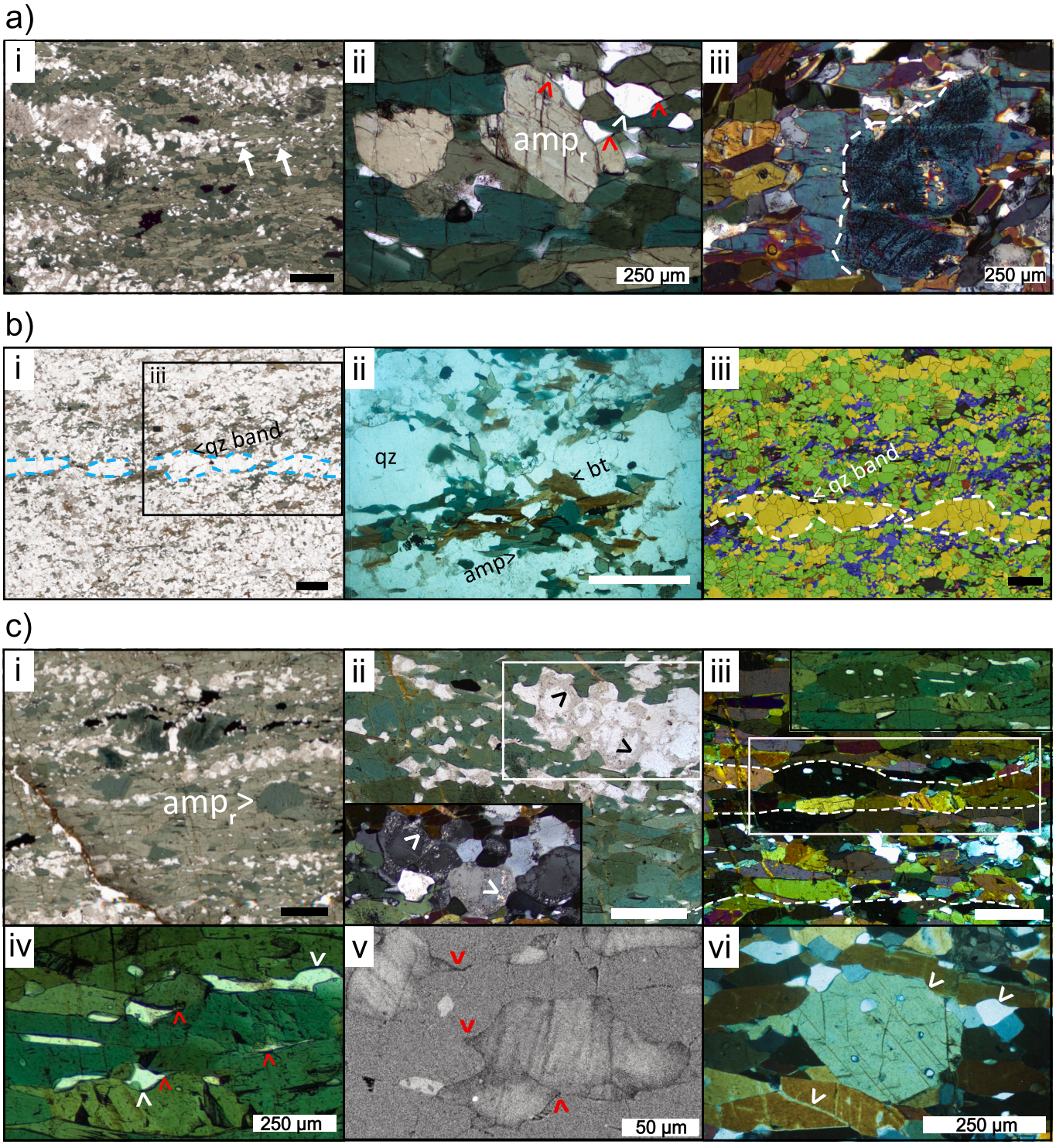

Fig. 6. Optical microstructures of domain 3 and 4 dyke (a & c) and gneiss (b), shown with thin section scans, photomicrographs in plane-polarised light (PPL) or cross-polarised light (XPL) where indicated, and EBSD false colour phase maps (see Fig. 5 for legend). (a) Dyke domain 3 T1 (AS2237); (i) elongate pl clusters and disseminated qz (white arrows), (ii) elongate amp (amp$_e$), more rounded, equant amp (amp$_r$), indentation (white arrows) and tails (red arrows), (iii) XPL asymmetric amp rim preferentially formed in the X direction (dashed lines denotes replacement front). (b) Gneiss domain 3 (AS2155); (i) semi-continuous qz band (ii) bt association with amp, (iii) pl-dominant matrix with large grains qz bands. (c) Dyke domain 4 T2 (AS2160); (i) elongate pl bands with elongate amp matrix and more rounded, equant amp (amp$_r$), (ii) heterogeneous pl seritisation, inset: XPL. (iii) XPL planar surface along aligned amp (dashed lines), (iv) qz indentation (white arrows) and tails (red arrows), (v) CL image of qz showing darker tails preferentially grown in X direction (red arrows) and (vi) photomicrograph showing amp-amp and amp-qz grain indentation (white arrows). Black scale bar: 1 mm and white bar: 500 μm, unless stated otherwise. (For interpretation of the references to colour in this figure legend, the reader is referred to the web version of this article.)

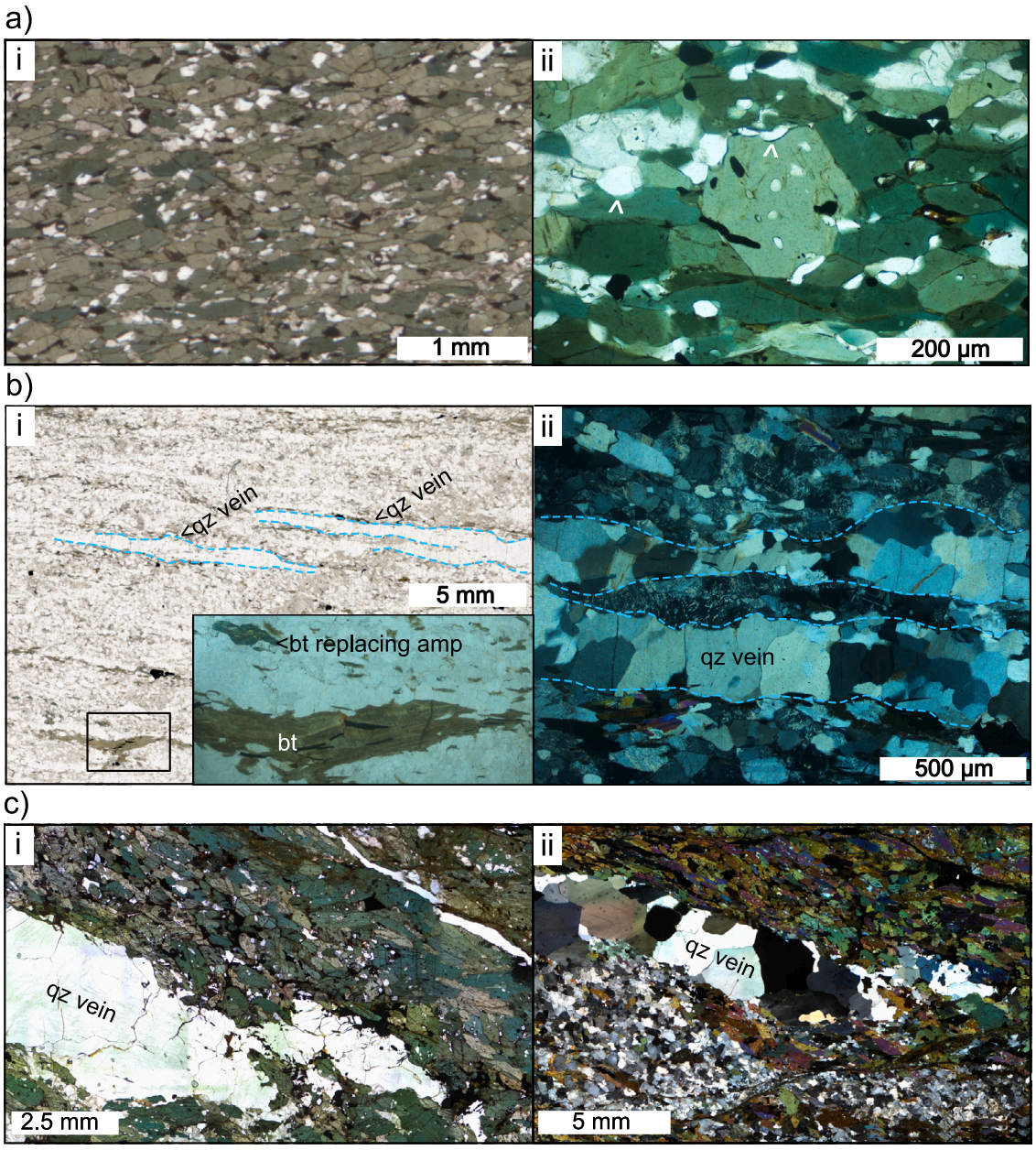

Fig. 7. Optical microstructures of domain 4 high strain dyke (a) and gneiss (b), and a mm wide quartz vein in dyke (c & d), shown in photomicrographs in plane-polarised light (PPL) or cross-polarised light (XPL) where indicated. (a) Dyke domain 4 T3 (AS2158); (i) qz, pl, ilm and czo are disseminated in amp matrix, (ii) asymmetric qz distribution around rounded, equant amp (amp_r) within elongate amp (amp_e) matrix, grain indentation (white arrows) and preferentially grown tails (red arrows). (b) Gneiss domain 4 high strain (AS2157); (i) fabric-parallel qz veins and bt seams, and (ii) different populations of qz: large-grained vein and smaller grains in pl-dominant bands. (c) Stitched photomicrograph of qz vein formed at local dyke-gneiss contact in (i) PPL and (ii) XPL. (For interpretation of the references to colour in this figure legend, the reader is referred to the web version of this article.)

clinozoisite and ilmenite are entirely disseminated within the 80% amphibole matrix, and grain size is largely unimodal as very few to no original large grains remain (Fig. 7a i). However, in common with domain 3 T1 and domain 4 T2 are specific microstructures such as indented grains, elongate, aligned tails and thin films, and aligned grain boundaries – despite the more uniform distribution of phases here (Fig. 7a ii).

Gneiss: Adjacent to T3 dyke, the gneiss mineralogy is similar to domain 3, albeit with marginally less amphibole. Here the gneiss has a strong fabric defined by 2 mm wide plagioclase domains and subparallel, continuous quartz bands (Fig. 7b i). Biotite forms semi-continuous layers, often adjacent to quartz veins and in places biotite is seen to replace amphibole (Fig. 7b ii, see also Fig. 6b ii). Plagioclase has a grain size of 0.1–0.2 mm and is only lightly altered to sericite, while subparallel, cm-long quartz bands (likely relict quartz veins) comprise larger 0.2–0.4 mm grains (Fig. 7b ii).

Quartz veins: In both the dyke and gneiss, where observed in thin section, quartz veins show a larger grain size compared to the surrounding matrix, of up to 2 mm and 0.5 mm respectively, and undulose extinction (Fig. 7b ii & c ii). In the shear zone centre, quartz veins are rare at sample scale in the dyke, however, in the high strain gneiss we see numerous quartz veins close together. The quartz veins in the gneiss show a variety of straight or undulatory boundaries, and biotite seams are often observed adjacent to quartz vein margins (Fig. 7b i).

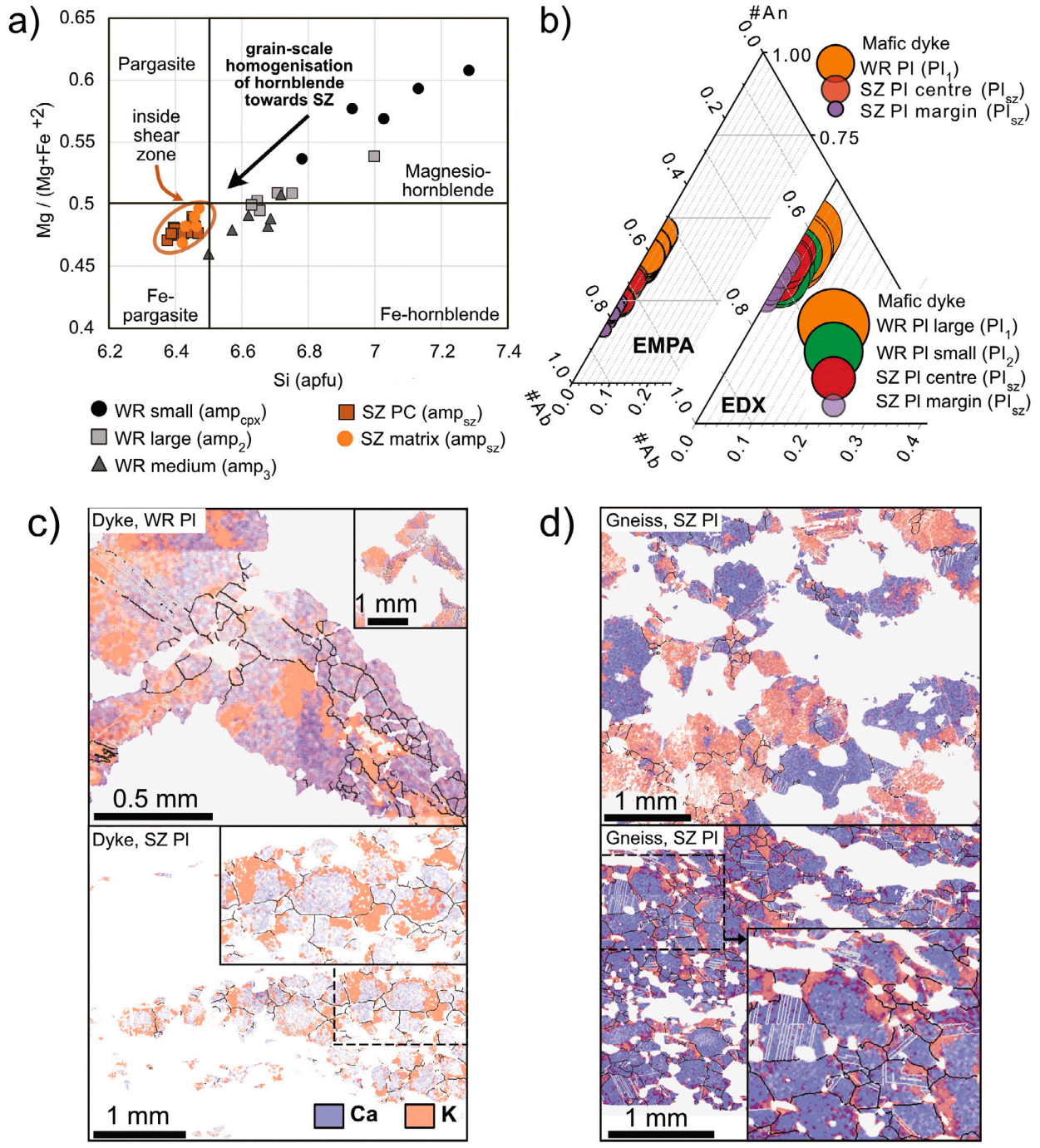

Fig. 8. Amphibole and plagiocalse chemistry in dyke and gneiss wall rock (WR) and shear zone (SZ) centre. (a) EMPA data for amphibole in dyke wall rock and shear zone (small grains < 100 μm, medium grains 0.1–02 μm). Si vs Mg# plot after Leake et al. 1997. We do not have chemistry data for amp_1 because of ilmenite inclusions, see text for details. (b) EMPA and EDX data for plagioclase in dyke wall rock and shear zone centre (small grains < 300 μm). (c & d) EDX chemistry maps for dyke (c) and gneiss (d) show asymmetrical, structural control on K-rich seritisation in the shear zone centre where blue = Ca and orange = K. High angle grain boundaries in black and twin boundaries in red. (For interpretation of the references to colour in this figure legend, the reader is referred to the web version of this article.)

4.5. Changes in mineral chemistry

4.5.1. Dyke: Amphibole composition is varied in wall rock but homogeneous in shear zone

In the dyke wall rock a range of amphibole chemistry exists across the amphibole populations, with compositions trending between magnesio-hornblende (WR small, 6.8–7.3 Si and 0.55–0.6 Mg#) and Fe-hornblende (WR medium, 6.5–6.7 Si and 0.450.5 Mg#, Fig. 8a). In contrast, the shear zone amphibole has a homogeneous Fe-pargasite composition. Within the wall rock, the magnesio-hornblende population most distinct from the shear zone is the small (<0.1 mm) amphibole observed in amphibole-quartz ± clinopyroxene areas (Fig. 5a iv). The Fe-hornblende population, closest in composition to the shear zone, is the medium (0.1–0.2 mm) sized amphibole which forms a margin between plagioclase and amphibole-quartz ± clinopyroxene areas (Fig. 5a iv). Between these two wall rock end-members is the

Table 2
Calculated estimates of H_2O content in dyke.

Domain	Domain 1	Domain 2	Domain 4	Domain 4
Type	**T0**	**T1**	**T2**	**T3**
Sample	AS2239	AS2153	AS2160	AS2158
Modal % Amp	60	70	75	80
H_2O in Amp (wt%)	2.8	2.8[a]	3.1	3.1[a]
H_2O in whole rock (wt%)	1.7	2	2.3	2.5
L_{H2O} per $m^3{}_{dyke}$	50.5	59	70	75
Relative increase (L/m^3)		+8.5	+19.5	+24.5

[a] AS2153 & AS2158 Amp wt% data from AS2239 & AS2160 respectively.

clear green amphibole associated with large (0.2–0.5 mm) grains, which has an intermediate hornblende composition (Fig. 8a).

4.5.2. Systematic change in plagioclase composition from wall rock to shear zone centre

In the dyke, where unaltered, large plagioclase grains exhibit an andesine (0.5–0.7 #Al) composition, while small plagioclase grains exhibit a slightly higher albite content andesine-oligoclase composition (0.6–0.75 #Al, Fig. 8b). In the shear zone centre, plagioclase is only lightly altered to sericite and overall has an andesine-oligoclase composition (0.65–0.85 #Al, Fig. 8b). However, the centre and margin of individual grains exhibit distinct chemistry, with grain margins comprising a slightly higher albite content (0.75–0.85 #Al) compared to the centre of grains (0.65–0.8 #Al, Fig. 8b). Fig. 8c illustrates how the spatial distribution of alteration of plagioclase to K-rich sericite in the wall rock compares to alteration in the shear zone centre. In the wall rock, large plagioclase is variably altered to sericite with a generally even distribution of alteration within grains, while small plagioclase is generally unaltered. In the shear zone centre, alteration to sericite occurs primarily at the margin of grains, and preferentially in the long axis of aligned, elongate plagioclase grains (Figs. 6c ii & 8c). The gneiss exhibits a similar alteration pattern to the dyke, with plagioclase grains variably altered to sericite in the wall rock, while in the shear zone centre sericite alteration is less and is observed primarily in the long axis of aligned, elongate plagioclase grains (Fig. 8d).

4.5.3. Change in H_2O content in dyke

The proportion of hydrous phases amphibole and clinozoisite increases in the dyke with strain and proximity to the shear zone (Table 1, see Section 4.4). To provide a minimum estimate of the increase in water needed to accommodate such changes, we use the wt% totals of EMPA analyses of amphibole to estimate the mean whole rock H_2O content in each sample (Supplementary materials Table S3; Stuart et al. 2018). The H_2O content in amphibole is 2.8 wt% in the wall rock and 3.1 wt% in the shear zone centre, which corresponds to an increase from 1.7 total wt% whole rock H_2O in the wall rock to 2.5 wt% H_2O in the shear zone centre (Table 2). To convert this to water content by volume gives an increase of 24.5 litres H_2O per m^3 of rock. This is a minimum estimate because, for simplicity, we do not account for clinozoisite modal increase and this calculation does not take into account the presence of any grain boundary fluid.

4.6. Quantitative changes in grain size with increasing strain

4.6.1. Dyke: With increasing strain, grain size and phase abundance decreases in plagioclase and increases in quartz and amphibole

The dyke grain size evolution is illustrated in Fig. 9a where small grain populations (amphibole < 80 μm, plagioclase < 300 μm and quartz < 100 μm) are highlighted as a subset to illustrate the different grain populations described in Section 4.4 and grain size is plotted in an area-weighted fraction histogram. In domain 1 T0 grain size is bimodal with significant proportions of amphibole, plagioclase and quartz both above and below the subset threshold (Fig. 9a). Small amphibole grains occur predominantly in amphibole-quartz ± clinopyroxene areas away from plagioclase, and > 80 μm amphibole is spatially associated with plagioclase. In domain 2 T1 fewer large grains are observed and plagioclase clusters are almost entirely small grains (Fig. 9a). In domain 4 T2, few small amphibole grains exist and they generally exist alongside individual small quartz and plagioclase grains close to plagioclase clusters. Instead, bands of > 80 μm amphibole exist away from plagioclase clusters. In domain 4 T3 quartz and plagioclase are generally below the subset threshold, while amphibole is generally above (Fig. 9a). Domain 4 amphibole and quartz grain size is generally unimodal, respectively above and below the subset threshold (Fig. 9a). Plagioclase is bimodal in domain 4 T2 due to very small individual plagioclase grains in the amphibole matrix adjacent to plagioclase clusters (Fig. 9a). In domain 4 T3, all plagioclase is now very small and disseminated within the amphibole matrix.

Overall, domain 1 area-weighted grain size distribution shows a large range but is dominated by small grains, however, with increasing strain amphibole and quartz median area-weighted grain size increases and the range decreases, to produce a more unimodal distribution in domain 4 (Fig. 9a). Plagioclase median grain size decreases slightly with increasing proximity to the shear zone, from 50 μm in the wall rock to ~ 35 μm in the shear zone centre (Fig. 9b). In contrast, quartz and amphibole median grain size increases with proximity to the shear zone, respectively from ~ 30 μm and ~ 25 μm in the wall rock to ~ 40 μm and ~ 80 μm in the shear zone centre (Fig. 9b).

4.6.2. Gneiss: In the shear zone grain size increases relative to wall rock

The gneiss grain size evolution is illustrated in Fig. 10a where small grains (amphibole < 120 μm, plagioclase < 200 μm and quartz < 100 μm) are highlighted as a subset to illustrate the different grain populations described in Section 4.4. Like in the dyke, domains 1 and 2 have a bimodal grain size with large, original grains and small reacted or recrystallised grains (Fig. 10a). Domains 3 and 4 matrix grain size is more unimodal, with plagioclase and amphibole grain size distribution almost entirely below 400 μm, however, quartz is an exception (Fig. 10a). Quartz veins that are ~ 1 mm wide and continuous over cm's have a larger grain size between 200-800 μm (Fig. 10a). Discontinuous quartz bands that are <0.5 mm wide and <1 cm in length have a grain size intermediate between small (< 100 μm) quartz disseminated within the plagioclase matrix and the quartz vein large grains.

The grain size of plagioclase, quartz and amphibole (where present) is ~ 50% greater in domains 3 and 4, compared to domain 1 (Fig. 10b). The median grain size in domain 1 is ~ 60, 35 and 350 μm for plagioclase, quartz and amphibole, respectively compared to ~ 100, 70 and 60 μm respectively in domains 3 and 4.

4.7. Changes in crystallographic orientation and shape fabric with increasing strain

4.7.1. Dyke

In dyke domain 1 T0 none of the main phases (amphibole, plagioclase, quartz) show any significant overall SPO or CPO (Fig. 11a). The aspect ratio of amphibole (large and small) and large plagioclase grains is 2.5 and 2.45, respectively. Quartz (large and small) and small plagioclase grains have an aspect ratio of 1.75 and 1.8, respectively. In domain 4 T2 and T3, whilst plagioclase and quartz still show no overall CPO, amphibole has a strong CPO with the *c*-axis [001] aligned in the X-direction, and the *a*-axis [100] parallel to the Z-direction, and all three main phases (quartz, plagioclase, amphibole) show a significant SPO with their long axes aligned in the X-direction (Fig. 11a). The aspect ratio of amphibole, plagioclase and quartz is greater here compared to domain 1, with aspect ratios of 2.85, 2.5 and 2, respectively, in domain 4 T2. Note that the SPO is strongest in these phases in the higher strain domain 4 T3, compared to domain 4 T2.

Although there is no overall CPO in domain 1 T0, locally, the intergrown, small grained amphibole-quartz ± clinopyroxene areas

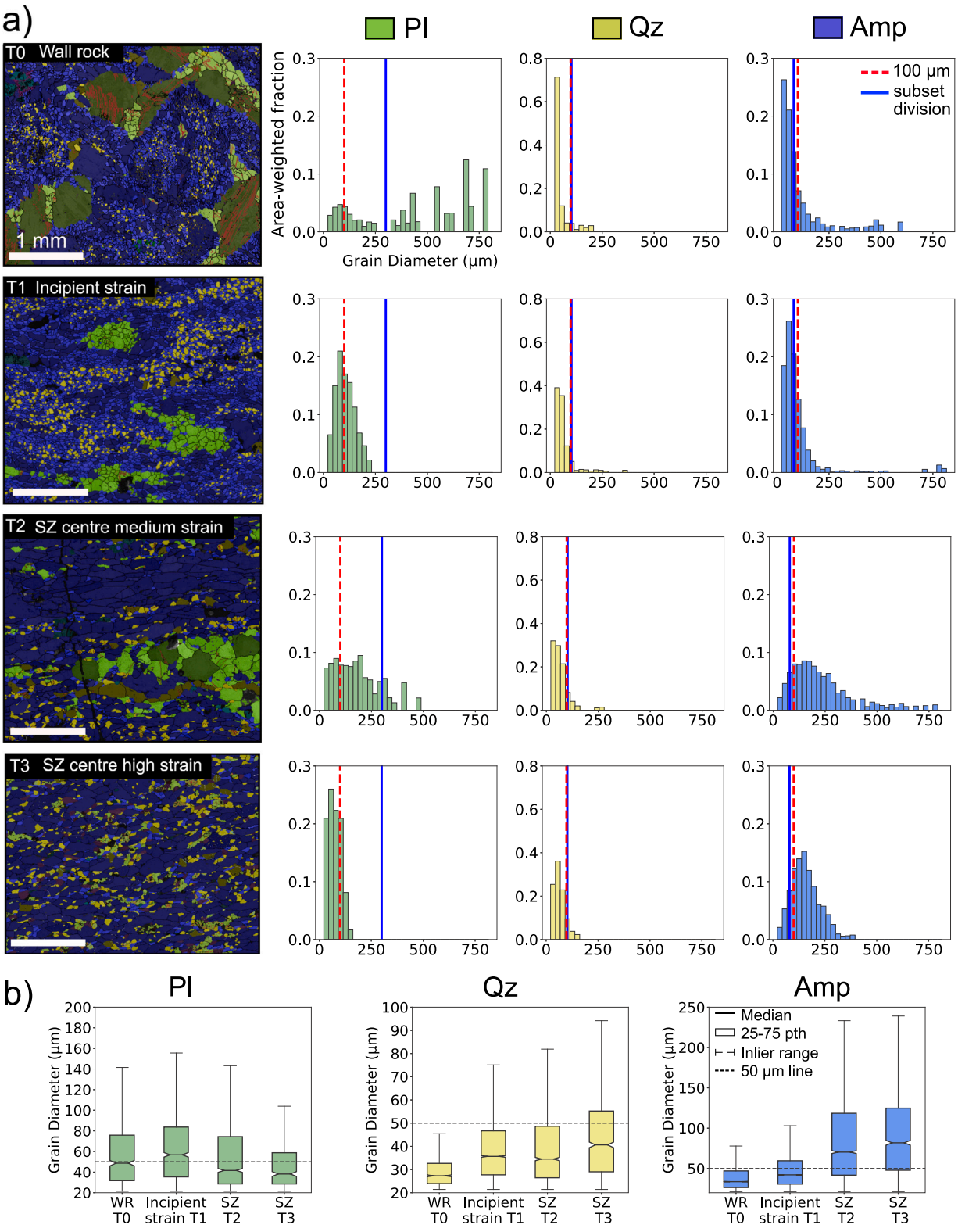

Fig. 9. Dyke grain size change with increasing strain and proximity to shear zone. (a) EBSD false colour phase maps showing the grain size and phase distribution change associated with increasing strain (T0-3), and corresponding area-weighted grain size fraction histograms. Small grain populations (pl < 300 μm, qz < 100 μm, amp < 80 μm) are highlighted in phase maps where amp = blue, pl = green and qz = yellow. Note increased phase mixing, homogenisation of grain size and fabric strength from left to right. Red line in histograms represents 100 μm, and blue line denotes the subset grain size threshold for each phase. WR = wall rock and SZ = shear zone. White scale bar: 1 mm. (b) Box and whisker plots for equivalent circle diameter grain size, with increasing strain and proximity to the shear zone. The whiskers extend to 1.5 times the interquartile range (IQR), and so do not display outlier data points. (For interpretation of the references to colour in this figure legend, the reader is referred to the web version of this article.)

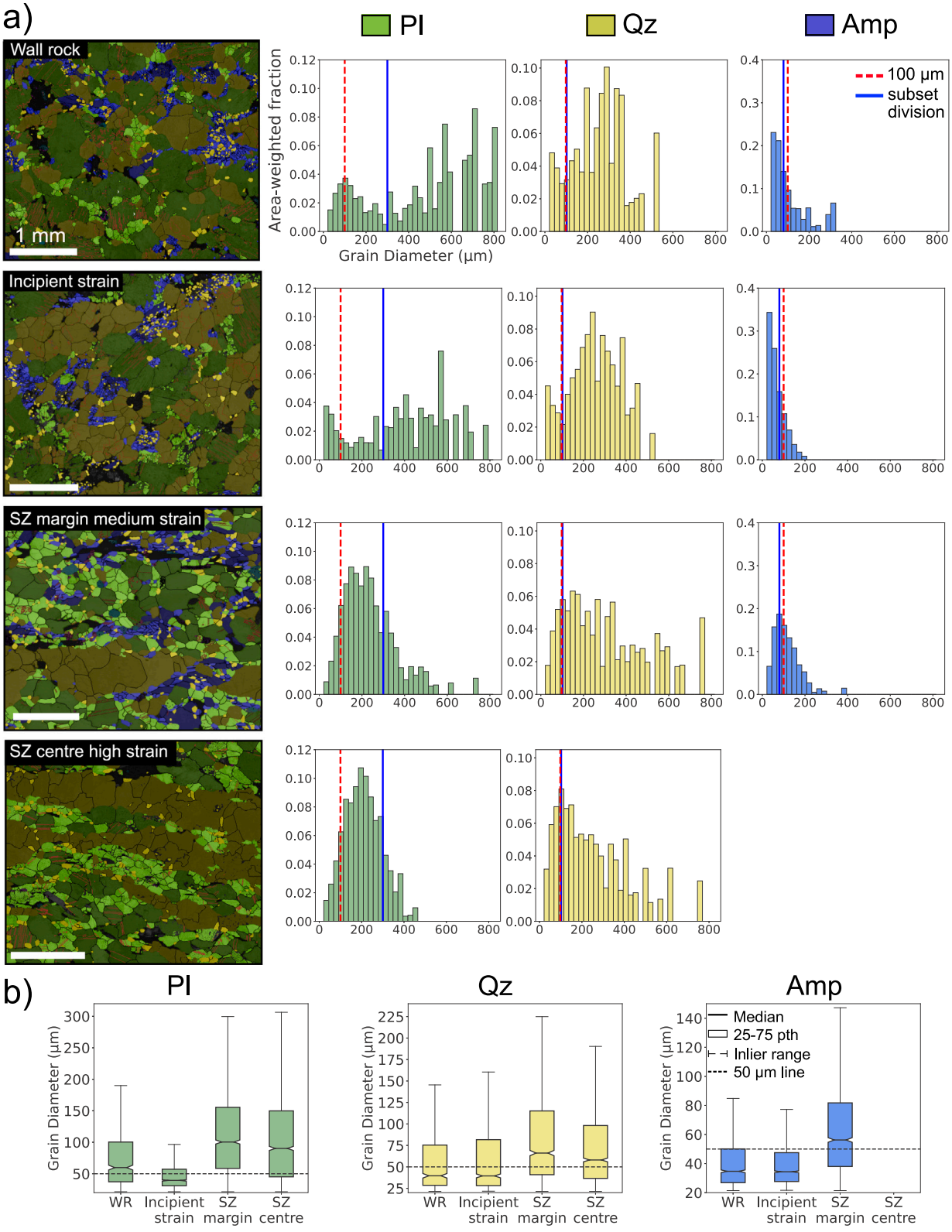

Fig. 10. Gneiss grain size change with increasing strain and proximity to shear zone. (a) EBSD false colour phase maps showing the grain size and phase distribution change associated with increasing strain, and corresponding area-weighted grain size fraction histograms. Small grain populations (pl < 200 μm, qz < 100 μm, amp < 120 μm) are highlighted in phase maps where pl = green, qz = yellow and amp = blue. Note increased phase mixing, homogenisation of grain size and fabric strength from left to right. Red line in histograms represents 100 μm, and blue line denotes the subset grain size threshold for each phase. WR = wall rock and SZ = shear zone. White scale bar: 1 mm. (b) Box and whisker plots for equivalent circle diameter grain size, with increasing strain and proximity to the shear zone. The whiskers extend to 1.5 times the interquartile range (IQR), and so do not display outlier data points. (For interpretation of the references to colour in this figure legend, the reader is referred to the web version of this article.)

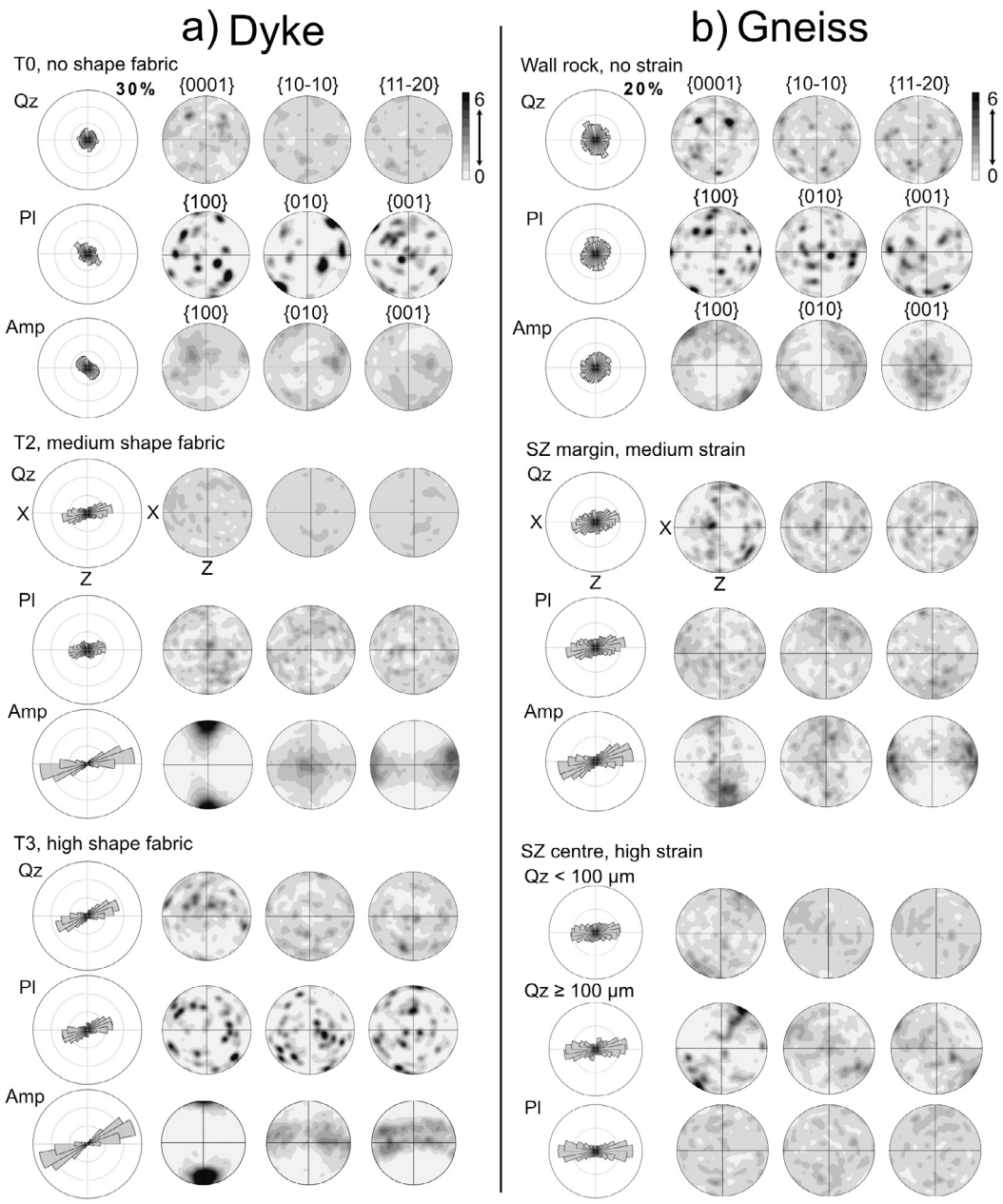

Fig. 11. Shape and crystallographic orientation data for the main phases (qz, pl and amp) showing microstructure change with increasing strain and proximity to shear zone in (a) dyke and (b) gneiss. Rose graphs display fitted ellipse angle as a proxy for shape-orientation and pole figures plot crystallographic-orientation. The shape fabric type (T0-3, dyke; low-high, gneiss) for each sample is shown. Dyke and gneiss SPO increases in all 3 phases with increasing strain and proximity to shear zone, but only amp develops a CPO with the exception of high strain gneiss where 'large' qz ≥ 100 μm also shows a CPO. Pole figure colour bars show multiples of uniform density (MUD) values with a range of 0–6, oriented data is shown in the XZ plane.

(Fig. 5a iv) exhibit for each area an area specific CPO with a clear crystallographic relationship to the parent clinopyroxene such that the amphibole CPO is the same as the parent clinopyroxene (Fig. 12a). In addition, the amphibole fringe formed between amphibole-quartz ± clinopyroxene areas and plagioclase locally exhibits a CPO that corresponds with the amphibole-quartz ± clinopyroxene area to which it is adjacent (Fig. 12a). Large grain populations (amphibole: 0.2–0.5 mm, plagioclase: 0.3–0.8 mm and quartz: 0.1–0.2 mm) exhibit significant, crystallographically-controlled intra-grain orientation change (7-8°), while small and medium grains (small amphibole and quartz <0.1 mm, medium amphibole: 0.1–0.2 mm and small plagioclase <0.3 mm) exhibit little to no (≤ 1°) intra-grain orientation change (Fig. 12b).

In domain 4 T2, neither the elongate matrix amphibole (0.1–0.3 mm) nor plagioclase (0.1–0.4 mm) show significant internal deformation (<2° within a single grain), however, remnant, large amphibole grains (1 mm) are randomly oriented compared to the amphibole matrix and possess 12° orientation change (Fig. 12c), similar to those in Domain 1 T0. In domain 4 T3, none of the main phases show any significant internal deformation, and large grains are absent (Fig. 12d).

4.7.2. Gneiss

Similar to dyke domain 1 T0, in the gneiss domain 1, none of the major phases (plagioclase, quartz, amphibole) show any significant overall SPO or CPO (Fig. 11b). The aspect ratio of (large and small) amphibole, plagioclase and quartz is 2, 1.8 and 1.65, respectively. In domain 3, whilst plagioclase and quartz still show no overall CPO, amphibole has a CPO with the *c*-axis [001] aligned in the X-direction, and the *a*-axis [100] parallel to the Z-direction, and all three main

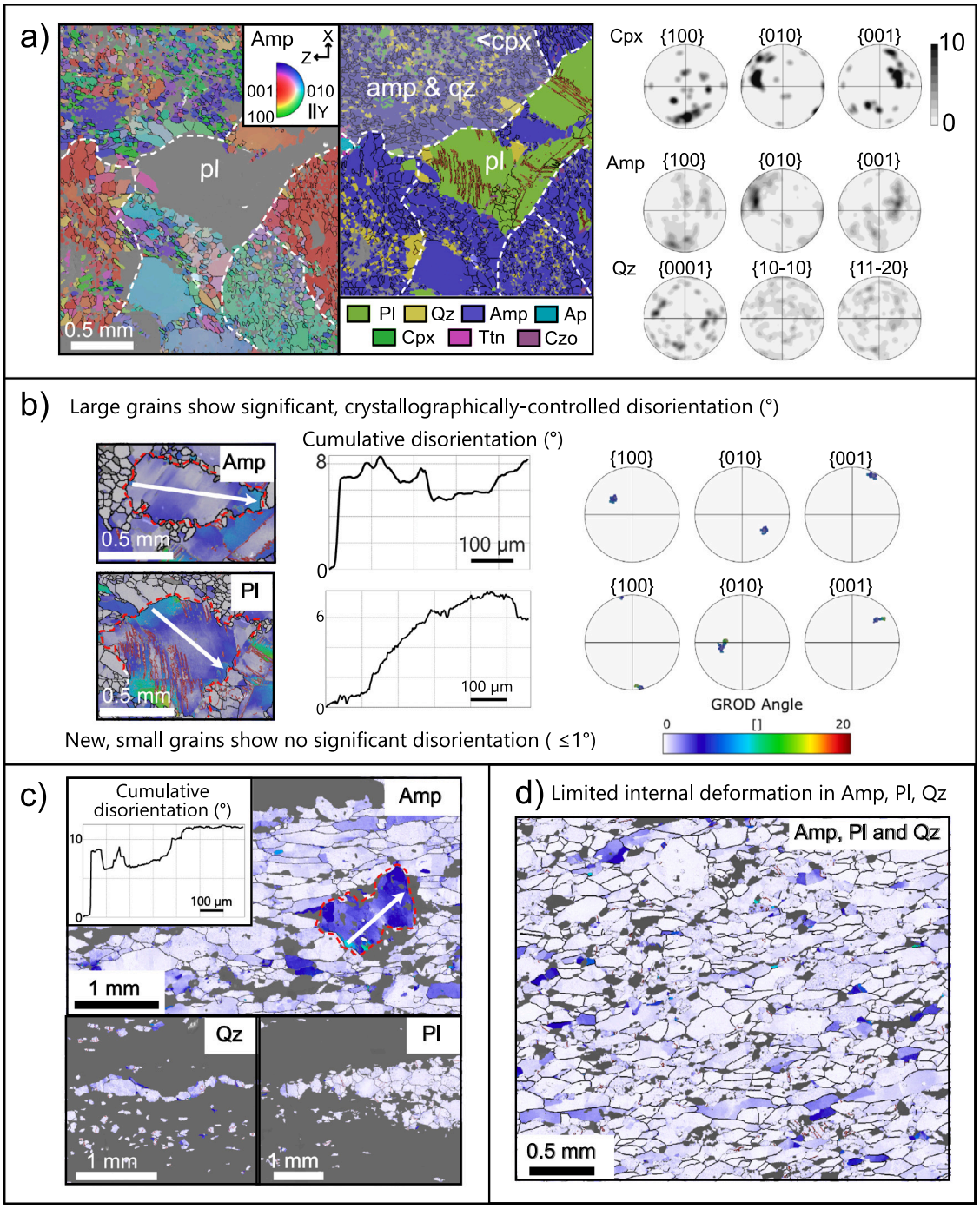

Fig. 12. Dyke: Crystallographic-orientation data and maps showing local, reaction-controlled CPO in wall rock amphibole and grain size-control on grain relative orientation deviation (GROD) i.e. intra-grain deformation. Maps are underlain by BSE maps. (a) Domain 1 T0 (AS2239); inverse pole figure (IPF) map shows local, area-specific orientation in amp (dashed lines). Shaded area in phase map (see Fig. 5 for legend) indicates the specific area plotted in pole figures, which shows local area-specific orientation of amp is related to parent cpx grain. Pole figure colour bars show multiples of uniform density (MUD) values with a range of 0–10. (b) Domain 1 T0 (AS2239); GROD maps and cumulative disorientation measurements show (i) 7-8° crystallographically-controlled internal deformation of large grains and <1° internal deformation of small, new grains. (c) Domain 4 T2 (AS2160); small, new grains show ≤ 2° internal deformation while large remnant amp shows >10° internal deformation. (d) Domain 4 T3; GROD map shows little to no internal grain deformation in amp, qz and pl. (For interpretation of the references to colour in this figure legend, the reader is referred to the web version of this article.)

phases (quartz, plagioclase, amphibole) show a significant SPO with their long axes aligned in the X-direction (Fig. 11b). In domain 4, plagioclase has an even stronger SPO but still no CPO, amphibole is absent and quartz has a stronger SPO in grains ≥ 100 µm, together with a CPO showing a rotated *c*-axis [0001] girdle (Fig. 11b). Quartz grains < 100 µm show a very faint rotated *c*-axis girdle. There is a slight increase in the aspect ratio of plagioclase and quartz in domain 4, compared to domain 1, with aspect ratios of 1.9 and 1.7, respectively.

In domain 1, again similar to dyke domain 1, the intergrown small grained amphibole-quartz areas (Fig. 5b) often exhibit locally an area specific CPO (Fig. 13a). Of the different grain size populations in T0, the large grain populations (plagioclase: 0.2–1 mm, quartz: 0.1–0.6 mm and amphibole: 0.1–0.4 mm) exhibit significant and systematic orientation change within individual grains (up to 14°, Fig. 13b). This corresponds to the undulose extinction observed optically (Section 4.4). In contrast, small grains (plagioclase: <0.2 mm, quartz: <0.1 mm and

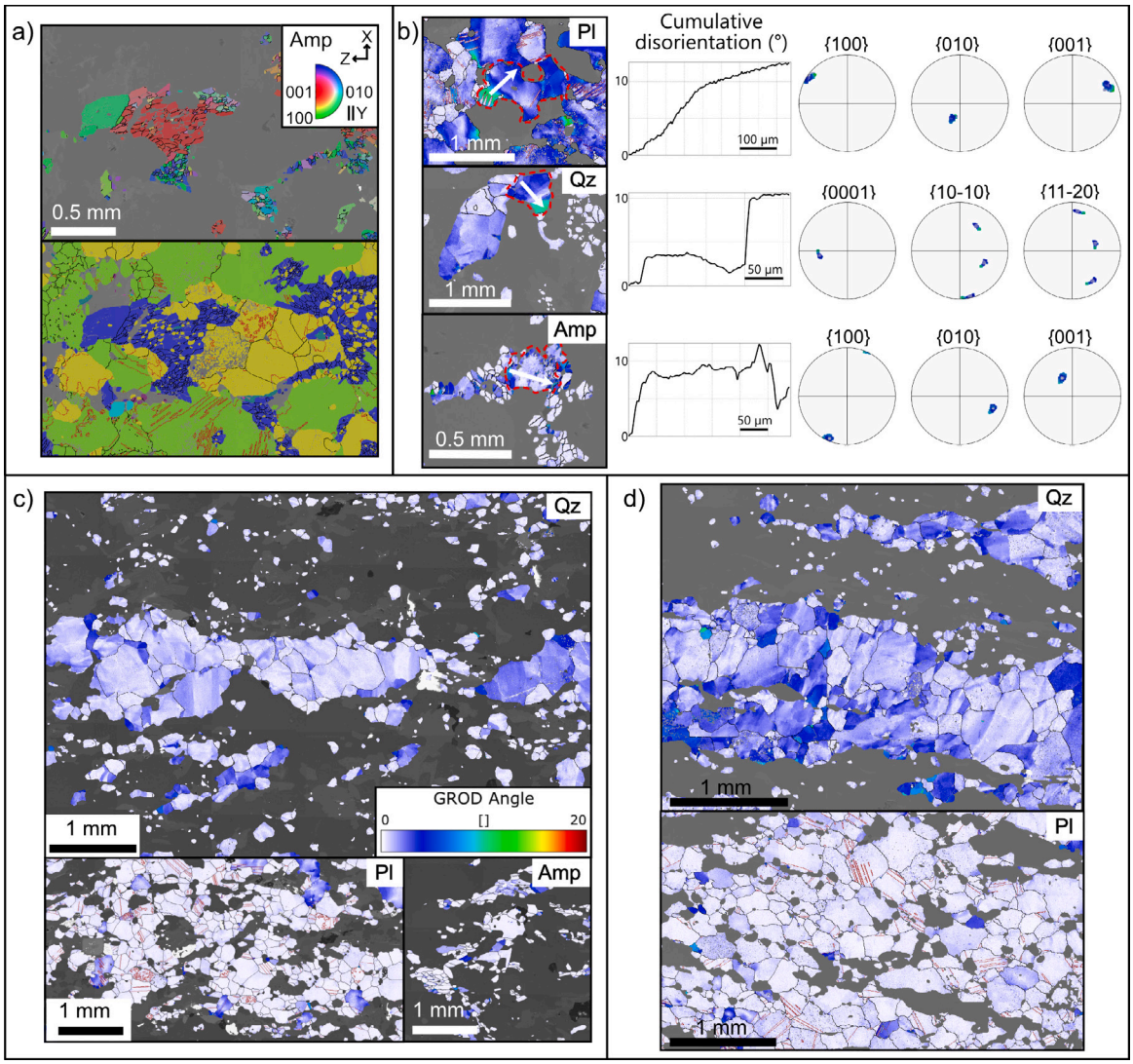

Fig. 13. Gneiss: Crystallographic-orientation data and maps showing local, reaction-controlled CPO in wall rock amphibole and grain size-control on grain relative orientation deviation (GROD) i.e. intra-grain deformation. Maps are underlain by BSE maps. (a) Domain 1 wall rock (AS2240a); inverse pole figure (IPF) map, with corresponding phase map (see Fig. 5 for legend), shows local area-specific orientation in amp. (b) Domain 1 wall rock (AS2240a); GROD maps and cumulative disorientation measurements show (i) 10-13° of crystallographically-controlled internal deformation in large grains and <2° of internal deformation in small, new grains. (c) Domain 3 medium strain (AS2155); GROD maps show minimal internal deformation of pl, amp and small qz, but up to 8° internal deformation in large qz. (d) Domain 4 high strain (AS2157); GROD map shows little to no internal deformation in pl and small qz, but up to 8° internal deformation in large qz. (For interpretation of the references to colour in this figure legend, the reader is referred to the web version of this article.)

amphibole: <0.1 mm) exhibit little to no orientation change within individual grains.

In domain 3, neither amphibole (<0.2 mm), plagioclase (0.1–0.4 mm), nor small quartz (<0.15 mm) show significant internal deformation (<2° within a single grain), however, semi-continuous bands of large (0.3–0.8 mm) quartz possess up to 8° intragranular orientation change (Fig. 13c). Domain 4 plagioclase and quartz show similar internal deformation signatures, but with more pervasive large quartz intra-grain deformation (Fig. 13d).

5. Discussion

5.1. The development of Badcall shear zone at amphibolite-facies conditions: Chemistry, hydration and phase change

Mineralogy within the shear zone is fully equilibrated to amphibolite-facies conditions (pargasite + andesine-oligoclase), in both the dyke and gneiss. This is in agreement with estimated P-T conditions: 510–660 °C and 5–8 kbar/500–800 MPa (Beach, 1973; Sills, 1982; Cartwright, 1990; Droop et al., 1999; Pearce and Wheeler, 2014). In the wall rock, chemically and/or microstructurally distinct grain populations delineate different reactions in space and time. To determine the relative timing of these populations, in this section we follow their evolution towards the shear zone centre where the most advanced hydration reactions occur.

In the dyke wall rock, the small (< 100 µm) amphibole in amphibole-quartz ± clinopyroxene areas (amp_{cpx} and qz_{cpx}) has the most distinct chemical composition with respect to the shear zone (Figs. 5a iv; 8a, Mg-hornblende and Fe-pargasite respectively). Amp_{cpx} show no significant internal deformation (<2°) within individual grains, and discrete amp_{cpx}-qz_{cpx} ± clinopyroxene areas largely preserve the crystallographic orientation of the ≥ 1 mm parent clinopyroxene grain (Fig. 12a). These grains are the result of static hydration of clinopyroxene at amphibolite-facies conditions, driving topotaxial replacement of clinopyroxene to produce amphibole that retains the orientation of the parent phase (e.g. Shannon and Rossi, 1964; McNamara et al., 2012; Lee et al., 2022). As outlined by Beach (1980), this replacement

reaction can also produce quartz, giving the general reaction:

$$cpx + \text{hydrous fluid} \rightarrow amp_{cpx} + qz_{cpx} + \text{hydrous fluid} \quad \text{(reaction 1)}$$

The presence of clinopyroxene, predominately in the centre of some amp_{cpx}-qz_{cpx} areas, indicates that here hydration is only partial and is localised even at the mm-scale.

Large (> 200 μm) amphibole exhibit a range of chemistry: end-members exhibit either dark ilmenite-speckled cores with clear green rims, or entirely clear green grains, and between these end-members, grains show partial replacement of ilmenite-cores with clear green amphibole (Fig. 5a ii–iii). We consider the ilmenite-speckled amphibole, amp_1, to be igneous, originally high temperature Ti-rich, amphibole that exsolved Ti to form ilmenite during cooling (e.g. Mongkoltip and Ashworth, 1983). We interpret the clear green amphibole rims and grains to be the result of static interface coupled replacement/dissolution–precipitation reactions, which replace amp_1 with chemically distinct amp_2 (Fig. 5a ii–iii, Putnis 2009). We did not obtain chemical data for amp_1 because of the ilmenite inclusions, however, the chemistry of amp_2 (hornblende, Hbl) is intermediate between amp_{cpx} (Mg-hbl) and the medium-sized (100 – 200 μm) amphibole population that has the closest chemistry to the shear zone, and which we define as amp_3 (Fe-hornblende, Fe-hbl, Fig. 8a). Amp_3 forms a reaction fringe between plagioclase and amp_{cpx}-qz_{cpx} ± clinopyroxene areas, where it indents and appears to replace plagioclase by preferential dissolution of plagioclase and precipitation of amphibole (Fig. 5a iv; Mérit et al. 2025). Similar to amp_{cpx} (Mg-hbl), amp_3 (Fe-hbl) does not exhibit crystal-plastic deformation features (i.e. no significant intragrain lattice distortions) and has a crystallographic orientation similar to the adjacent amp_{cpx} area (Fig. 12a & b). The chemistry of plagioclase also changes, through the recrystallisation of large original pl_1 grains to small new pl_2 grains (Fig. 5a ii–iii; bimodal grain size, Fig. 9a). Pl_2 (andesine-oligoclase, Ab_{60-75}) are less altered by sericite and exhibit a ~ 5% higher albite content, compared to pl_1 (andesine, Ab_{55-70}, Fig. 8b EDX).

The gneiss wall rock comprises plagioclase and amphibole populations which exhibit the same spatial and crystallographic relationships observed in the dyke, with the exception of igneous amp_1 and with a lower amphibole content overall (10 modal % compared to 60 modal % in dyke wall rock, Table 1; Figs. 5b i–iii; 11b; 13a). Areas of amphibole-quartz (anolgous to amp_{cpx}), with a reaction fringe (analogous to amp_3) at the margin of plagioclase, appear to have also formed through reaction 1, where pre-existing clinopyroxene reacts with fluid to form amphibole ± quartz (Fig. 5b iv). The ~ 5% observed chlorite is texturally late and represents static alteration of amphibole, perhaps related to the greenschist-facies 'late Laxfordian', or otherwise named 'Assyntian', event that followed 'Laxfordian' amphibolite-facies deformation (Table 1; Holdsworth et al. 2020) .

Reaction 1 requires fluid input and indicates influx of fluid prior to significant deformation. While some large grains exhbit internal deformation (see Section 5.3 below), the preservation of local orientation of amp_{cpx}-qz_{cpx} areas and amp_3 reaction fringes indicate the lack of significant strain in the wall rock since these reactions occurred. Next, we outline the evolution of grain populations and phase abundance towards the shear zone centre, which correspond to an increase in strain and hydration.

In domain 2, grain populations similar to those in T0 dyke exist in T1 dyke and low-medium strain gneiss, however, here distinct areas of grain populations are elongate parallel to lineation (Fig. 5c & d). Reaction 1 is complete and no clinopyroxene remains, which means fluid is no longer absorbed and it can instead facilitate deformation (Table 1). The presence of asymmetric quartz beards in pressure shadows indicates precipitation of material from such a fluid (Fig. 5c iii). Preferentially aligned matrix amphibole envelop and indent (i.e. dissolve) clusters of small, recrystallised plagioclase, while elongate bands of (clinopyroxene-absent) amp_{cpx}-qz_{cpx} areas exist away from such clusters (Fig. 5c i inset & ii).

We propose that the observed progressive replacement of plagioclase by amphibole, by apparently coupled dissolution–precipitation processes, explains the 10–25 modal % increase in amphibole and decrease in plagioclase in deformed dyke, relative to undeformed T0 (Table 1; Grund et al. 2025, Mérit et al. 2025). A complete characterisation of this process is beyond the scope of this study, however, it likely involves both material transfer and chemical exchange in the presence of fluid. Overall, the original andesine pl_1 (Ab_{55-70}) clusters reduce in both grain size and cluster size through reaction-driven grain size reduction from original large grains to new, smaller andesine-oligoclase pl_2 (Ab_{60-75}) grains, and through the replacement of plagioclase by amphibole associated with dissolution–precipitation processes.

In domains 3 and 4 (shear zone margin and shear zone centre), amp_{cpx}-qz_{cpx} bands are absent in dyke T1 and T2, and the spatial distribution of phases is significantly changed. Here, preferentially aligned, elongate amphibole form continuous bands away from plagioclase clusters, and quartz and smaller amphibole exist predominantly in the tails of plagioclase clusters or large amphibole porphyroclasts (Figs. 6a i & c i; 9a). Mineral chemistry shows that shear zone matrix amphibole (amp_{SZ}, Fe-pargasite) is entirely distinct from amphibole populations in wall rock T0 (Fig. 8a, Mg- to Fe-hornblende). We interpret amp_{SZ} to form from a continuation of the dissolution–precipitation processes identified in domains 1 and 2 (wall rock and incipient strain), where infiltrating fluids interact with the rock. Through this process, amp_{SZ} replaces earlier amphibole populations (amp_{cpx} and $amp_{1\text{-}3}$) due to their meta-stable composition and/or non-optimal grain orientation, which promotes preferential dissolution or precipitation of material according to grain orientation relative to sites of high stress (dissolution) or low stress (precipitation; Kamb 1959). Ilmenite-speckled amphibole porphyroclast cores remain in places, however, here the clear green rims bear the same chemistry as the matrix amp_{SZ} (Fe-pargasite). The fact that the wall rock amphibole populations evolve from Mg- and Fe-hornblende, towards but staying distinct from the shear zone pargasite (amp_{SZ}, Fig. 8a), suggests that within the shear zone the rock fully equilibrated to the prevailing P-T-fluid conditions during deformation but the wall rock did not.

Plagioclase chemistry is also distinct in the shear zone, with an oligoclase-andesine composition ~ 10%–15% higher #Ab compared to the wall rock andesine pl_1 (Fig. 8b; Ab_{65-85} and Ab_{55-70} respectively). The shear zone centre plagioclase, pl_{SZ}, is asymmetrically zoned, with an oligoclase-andesine composition (Ab_{65-80}) at the centre of grains but often a higher #Ab oligoclase composition (Ab_{75-85}) at their margin (Fig. 8b). EDX maps show how the distribution of pl_{SZ} sericite alteration is structurally controlled in both the dyke and gneiss, where alteration occurs predominantly in the long axis of grains grown preferentially in the X-direction (Fig. 8c & d). Given the microstructural similarities between dyke T1 and T2 in domains 3 and 4, we propose that amphibole and plagioclase chemistry in shear zone centre is comparable to that in the shear zone margin.

Overall, dyke wall rock amphibole populations are consumed and replaced by chemically distinct amphibole in the shear zone (Fig. 8a). Plagioclase is also distinct in the shear zone compared to the wall rock, with a chemical composition that is higher in albite content in the shear zone, particularly in the long axis of grains aligned in the X-direction (Fig. 8b-d). The absence of clinopyroxene in domains 2–4, and the increase in amphibole and clinozoisite in domains 3 and 4, indicates not only a correlation between hydration, reactions and strain as detailed previously by Beach (1980), but importantly also requires the introduction of external fluid (Table 1).

5.2. Fluid influx: quartz vein abundance coincides with increase in hydration and strain

Tatham and Casey (2007) established a macro-fabric strain gradient from <1 in the shear zone margin, to 15 in the shear zone centre, based on the rotation of macro fabric in the gneiss (Fig. 1b). Our maps of

shape fabric intensity show deformation in the dyke at outcrop scale, even in domain 2 where the dyke remains undeformed at map-scale (Figs. 1b; 4). In domain 2 the distribution of strain is heterogeneous, with discrete, anastomosing bands of T1 that envelop the dominant undeformed T0 lenses, which comprise >60% of the dyke here (Figs. 2c i & d i–ii; 4d). From domain 2 to domain 4, strain in the dyke becomes more pervasive and homogeneously distributed. Planar T1 shape fabric dominates >60% of the dyke in domain 3, and only limited T0 lenses exist (Figs. 3a i; 4). In domain 4 100% of the dyke exhibits a planar fabric, 60% of which comprises the higher strain T2 (Figs. 3b ii; 4). The presence of remnant clinopyroxene in only T0 means hydration is incomplete in T0 dyke (Fig. 5a iv; Table 1). In contrast, in domains 2–4 dyke T1-3, absence of clinopyroxene suggests that hydration reaction 1 is complete. In domain 4 dyke T2-3 the greatest abundance of hydrous phases is observed (Table 1, amphibole and clinozoisite). Therefore, with increasing proximity to the shear zone we observe an increase in shape fabric intensity and strain, which is correlated with an increase in hydrous phases and dyke H_2O content from 1.7 to 2.5 wt% (Table 2; Beach 1980, Ramsay 1980, Putnis 2021, Grund et al. 2025). Based on hydrous phase modal percentages we calculate that an influx of at least 8.5 and 19.5–24.5 L_{H2O} per m^3 dyke is needed to account for the increased hydration in domain 2 T1 (incipient strain) and domain 4 T2-3 (shear zone centre), respectively (Table 2, see Section 4.5.3). These estimations are in line with suggested influx of fluid proposed by Beach (1980) for similar shear zones in NW Scotland.

The presence of hydrated mineral assemblage, increased shape fabric intensity and strain with proximity to the shear zone is also correlated with the increased abundance of syntectonic quartz veins (Fig. 4 b-d, fabric-parallel or subparallel, 0.5–20 mm wide and up to 60 cm long). In the dyke shape fabric maps, all but one quartz vein are observed in either the shear zone margin or shear zone centre (domains 3 and 4), and all quartz veins are observed within shape fabric T1-3 (i.e. not observed in T0). Due to the similarity in grain habit between a dyke quartz vein (Fig. 7c) and quartz bands in gneiss domains 3 and 4 (Figs. 6b; 7b), we consider semi-continuous to continuous coarse quartz bands in the gneiss to represent deformed quartz veins. This suggests quartz veins are significantly more abundant in the gneiss, as a number of these deformed veins are present within individual thin sections (Figs. 6b iii; 7b).

Quartz veins are known to be related to fluid influx (Sibson, 1981, 1994; Bons et al., 2012), and syntectonic quartz-carbonate veins have been previously reported in the nearby Gairloch shear zone (Beach, 1980). We interpret the quartz veins to represent episodes of local brittle failure (in otherwise viscous flow), which produced fractures that were subsequently filled through the precipitation of quartz from fluid (Yardley, 1983; Bons et al., 2012; Hayman and Lavier, 2014; Fagereng et al., 2018). In this way, the increase in syntectonic quartz veins with proximity to the shear zone reflects localised fluid-infiltration via fractures at the time of deformation (Figs. 3; 4; 7b & c). The spatial coincidence of hydration, strain and quartz vein abundance calls for causal relationships, and suggests deformation associated with the shear zone is facilitated by fluid.

We highlight that the quartz veins we observe here are small, discrete and discontinuous, relative to extensive quartz vein networks typically observed at shallower depths (e.g. Williams and Fagereng 2022). The source of the quartz may be internal and/or external: in part derived from fluid and/or derived entirely from the host rocks. Previous authors have proposed the introduction of fluids to the mid-crust during earthquakes, i.e. 'seismic pumping' proposed by Sibson (1981, 1994), and mid-crustal quartz veins have been found to bear an isotopic signature which indicates meteoric-fluid (McCaig, 1988; Stenvall et al., 2020; Gottardi et al., 2024). Other potential sources of fluid are magmatic or metamorphic.

5.3. Remnant signatures of dislocation creep in wall rock contrast dominance of dissolution–precipitation creep within shear zone

5.3.1. Signatures and timing of dislocation creep in wall rock

In the wall rock there is no overall CPO or SPO (Fig. 11), however, large (~ 1 mm) plagioclase, amphibole and (>0.1 mm) quartz grains in gneiss and dyke preserve signatures of crystal-plastic dislocation creep deformation accumulated by strain in the wall rock. These include undulose extinction, crystallographic-controlled internal deformation of grains, and limited subgrains (dyke, Fig. 12b; gneiss, Fig. 13b). We know that the wall rock did not experience significant deformation since reaction 1 occurred because amp_{cpx} and amp_3 retain local CPO related to their parent grain (dyke, Fig. 12a; gneiss, Fig. 13a), and the distribution of large and small plagioclase grains is not structurally controlled. The preserved signatures of dislocation creep in large plagioclase, amphibole and quartz reflect the history of the wall rock as being relatively strong, prior to fluid-infiltration and reaction-driven grain size reduction (see Section 5.1). Because partial hydration reactions have occurred in the wall rock (Section 5.1), we know that the hydration associated with the shear zone extends further from the shear zone than does significant deformation. Therefore, hydration likely preceded the deformation associated with the shear zone in domains 2–4, where a greater degree of hydration allows for the activity of dissolution–precipitation creep and associated weakening of the rock.

5.3.2. Deformation is dominated by dissolution–precipitation creep

At the microscale, deformed dyke and gneiss show with strain a development of SPO in all major phases and CPO in amphibole (Fig. 11), despite a lack of internal deformation of grains (with the exception of bands of large quartz in the gneiss, and remnant porphyroclasts in the dyke; Figs. 12c & d; 13c & d). The development of SPO without significant internal deformation of grains is consistent with numerical models that produce grain shape change during grain-size-sensitive deformation processes that involve the movement of material from a surface of relatively high stress to a surface of lower stress. This can occur by strictly diffusive processes (Gardner and Wheeler, 2021), or by dissolution–precipitation creep where material is dissolved at surfaces of high stress, transported in grain boundary fluid and subsequently precipitated in areas of low stress (Malvoisin and Baumgartner, 2021). The development of SPO in the absence of internal grain deformation is consistent with microstructural and experimental studies which attribute deformation to dissolution–precipitation creep (Wintsch and Yi, 2002; Díaz Aspiroz et al., 2007; Stokes et al., 2012; Marti et al., 2018; Lee et al., 2022).

The development of CPO in amphibole in both dyke and gneiss without significant internal deformation of grains indicates that CPO formed by means other than dislocation creep. Kamb (1959) observes anisotropic grain growth, where 'the preferred orientation is that which minimises the chemical potential required for equilibrium across the plane normal to the greatest principal pressure axis. Thus, the weakest axis of a crystal (e.g. *c*-axis of calcite) tends to align with the greatest principal pressure axis, or axes, while the strongest axis (e.g. *c*-axis of quartz) tends to align perpendicular thereto'. Preferential growth in the long axis of amphibole (an elastically anisotropic mineral) creates CPO in favourably orientated grains, accompanied by associated rigid body rotation through the dissolution (or truncation) of surfaces of unfavourable crystallographic-orientation and precipitation on favourably oriented grain surfaces (Fig. 6c vi). Similar signatures have been identified where pre-existing chemical zoning in grains is preferentially truncated by dissolution as a fabric is formed during deformation (Wintsch and Yi, 2002; Stokes et al., 2012; Wassmann and Stöckhert, 2013; Giuntoli et al., 2018; Moore et al., 2024; Mérit et al., 2025). This aids the alignment of grain boundaries in the X-direction, creating planar surfaces which extend across several grains (Fig. 6c iii), which look similar to weak 'sliding surfaces' produced during numerical modelling of diffusion processes (Gardner and Wheeler, 2021). In this

way, a microstructure favourable for co-operative grain boundary sliding develops. Semi-continuous aligned biotite seams in gneiss domains 3 and 4 (Fig. 7b i) may behave similarly. The lack of CPO development in plagioclase and, in the dyke, quartz, is consistent with deformation by dissolution–precipitation creep because plagioclase and quartz are not significantly anisotropic minerals and as such they are not expected to produce a CPO in the same way as amphibole. In contrast, SPO does not rely solely on crystallographic control and therefore all three main phases develop a SPO that appears to reflect their anisotropy to some degree; in order of highest mineral anisotropy to least anisotropy, aspect ratios are 2.85, 2.5 and 2 in dyke T2 amphibole, plagioclase and quartz, respectively.

The progressive replacement of amp_1 by amp_2 from grain edge to grain centre in all four domains is a distinct signature of coupled dissolution–precipitation. Reactions in dyke domain 1 T0 occur statically and there is no structural control on the dissolution–precipitation interface (Fig. 5a ii–iii). However, with increased strain in T1-3, asymmetric amp_2 rims grow preferentially in the X-direction (Fig. 6a iii), implying that material is transported from high stress surfaces (Z-direction) to low stress surfaces (X-direction, i.e. Wintsch and Yi 2002). The homogeneous amphibole chemistry in dyke domain 4 T2, compared to the range in chemistry observed in dyke domain 1 T0, suggests that dissolution–precipitation processes have replaced grains entirely – no zoning is preserved except for infrequent amp_1 porphyroclast cores (Fig. 8a). Similarly, the structurally-controlled composition of pl_{SZ} and the chemically distinct quartz tails in dyke T2 suggest mobilisation of material through dissolution–precipitation creep, which promotes preferential precipitation/growth in the long axes of grains aligned in the X-direction (Figs. 6c v; 8c & d; Wintsch and Yi 2002, Stokes et al. 2012, Wassmann and Stöckhert 2013, Trepmann and Seybold 2019, Giuntoli et al. 2022, McNamara et al. 2024, Wintsch et al. 2024, Mérit et al. 2025). The microstructure of individual quartz grains amongst amphibole matrix in dyke domains 3 and 4 suggests quartz indents (dissolves) amphibole in the Z-direction, while simultaneously developing thin tails in the X-direction (Fig. 6a ii & c iv–vi). Thin quartz films between aligned amphibole grains are also very distinctive, likely formed through the transport and precipitation of material along grain boundaries.

At outcrop scale, the intensity of shape fabric reflects the activity of dissolution–precipitation creep. In domain 2 dyke the limited presence of T1, anastomosed around elongate lenses of T0, illustrates the heterogeneous and limited distribution of hydration and activity of dissolution–precipitation creep outside of the shear zone (Fig. 4d). In domain 3, the m-wide regions of planar T1 dyke fabric suggest that hydration and the activity of dissolution–precipitation creep is much more pervasive in the shear zone margin. Finally, in domain 4 where planar fabric and strain is homogeneously distributed, we find that the entire shear zone centre is sufficiently hydrated, weak and able to deform pervasively by dissolution–precipitation creep.

5.3.3. Minor component of dislocation creep in large vein quartz and amphibole grains

As outlined above, the microstructure in deformed dyke and gneiss indicates a dominance of dissolution–precipitation creep and, with the exception of rare, large amphibole porphyroclasts in the dyke and bands of large quartz in the gneiss, a general lack of dislocation creep signatures. In deformed dyke and gneiss matrix we do not observe features that are known to be associated with dislocation creep, such as subgrains, grain size reduction by subgrain rotation (dynamic recrystallisation), core-mantle structures, bending of crystal lattices or a slip system-controlled CPO (Figs. 12 c & d; 13 c & d; Trimby et al. 1998, Prior et al. 2002, Piazolo et al. 2002, Passchier and Trouw 2005, Halfpenny et al. 2006). It is only the large grains that exhibit some component of dislocation creep.

In the dyke, internal deformation of large amphibole porphyroclasts is similar in magnitude to those in the wall rock (>10° cumulative disorientation), while the surrounding shear zone matrix has little to no internal deformation (Fig. 12c & d). We consider these grains to represent amp_1 or amp_2 grains, which have survived from pre-hydration deformation, or have experienced grain size strain partitioning due to their larger grain size. Grain-size-sensitive dissolution–precipitation creep is most effective at small grain sizes, so more strain will be accommodated by the smaller matrix grains, and larger porphyroclasts are less affected. In addition, the large grain porphyroclasts are often poorly aligned crystallographically, so rates of dissolution and precipitation will be less effective. Similar to the way in which preservation of large porphyroclasts is expected if grain-size-sensitive grain boundary sliding accommodated by dislocation creep or dislocation glide (Dis-GBS) is active (Warren and Hirth, 2006), here large porphyroclasts of amphibole are preserved as smaller matrix grains accommodate strain more easily at lower stresses – producing some grain size strain partitioning. In domain 3 and 4 gneiss, larger grained quartz bands exhibit some internal deformation (Fig. 13c & d), which could reflect grain size dependent partitioning of strain, or a rheological contrast between the surrounding plagioclase matrix and the quartz bands at the temperature of deformation. A weaker surrounding matrix would exert higher stress on the quartz bands, enabling deformation by dislocation creep.

5.4. Proposed shear zone model: Strain localisation by localised fluid-infiltration and activation of dissolution–precipitation creep

5.4.1. Stage 0: Strong, anhydrous crust deformed in dislocation creep regime

Prior to shear zone initiation, granulite-facies anhydrous pyroxene bearing-quartzofeldspathic gneisses form during the 'Badcallian' tectonometamorphic event c. 2800–2700 Ma between 750-990 °C and 7–11 kbar (Sutton and Watson, 1950; Park, 1970; Cartwright and Barnicoat, 1987; Sills and Rollinson, 1987; Corfu et al., 1994; Goodenough et al., 2013). A dolerite dyke (plagioclase, clinopyroxene, amphibole and minor quartz), part of the Scourie dyke swarm, intrudes under conditions of 450–500 °C and 5–7 kbar, 2400–1900 Ma between the amphibolite-facies 'Inverian' and 'Laxfordian' tectonometamorphic events (Sutton and Watson, 1950; Tarney, 1963; Park and Tarney, 1987). Far-field 'Laxfordian' stress produces minor, dislocation creep regime, deformation in the coarse 1 mm grain size anhydrous gneiss and dyke, producing internal grain deformation and few subgrains (Sections 4.7 and 5.3.3; Figs. 5a & b; 12b; 13b). The preservation of original igneous, isotropic dyke T0 microstructure indicates very minor strain overall (Stage 0, Fig. 14).

5.4.2. Stage 1: Brittle failure drives localised fluid ingress and hydration reactions, locally weakening the crust

We hypothesise that a high strain rate event (such as an earthquake) in the upper-crust extends into the mid-crust brittle–ductile transition zone and, where the relatively homogeneous crust fails in a brittle manner, introduces fluid into fractures (Stage 1, Fig. 14; i.e. Giuntoli et al. 2018, Putnis 2021, Zertani et al. 2023, Moore et al. 2024). Where fluid is introduced to anhydrous crust bearing clinopyroxene, it permeates along grain boundaries to drive initial hydration reaction 1 ($cpx + hydrous\,fluid \rightarrow amp_{cpx} + qtz_{cpx} + hydrous\,fluid$), weakening the rock through significant reduction in grain size of amphibole and quartz from 1 mm to < 100 μm (Fig. 5a iv; wall rock, Fig. 9; Stage 1, Fig. 14). Where reaction 1 is incomplete and remnant clinopyroxene remains, continued reaction will consume, and limit the availability of, fluid such that sufficient fluid is not available to initiate dissolution–precipitation creep. Where reaction 1 is complete (clinopyroxene is entirely consumed), and grain boundaries are sufficiently wetted, these areas begin to deform by dissolution–precipitation creep, switching the dominant deformation regime from dislocation creep to dissolution–precipitation creep (Section 5.3). Strain subsequently localises in these areas because deformation in the dissolution–precipitation creep regime requires significantly less stress compared

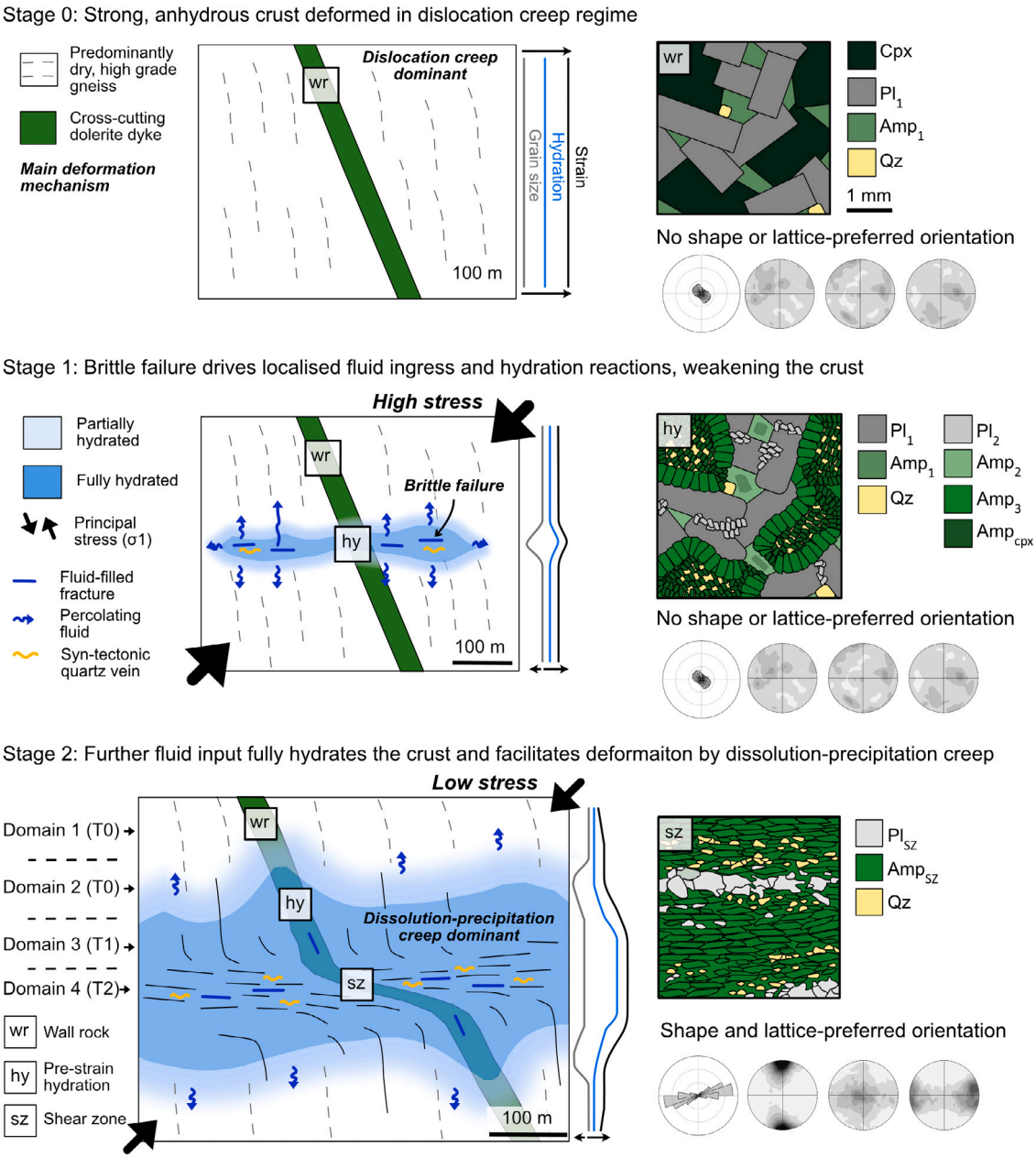

Fig. 14. Schematic model of the evolution of the shear zone in map view (left) and associated microstructural development in the dyke (right). Microstructural development figures illustrate changes in phase, grain size and texture with strain, and the corresponding change in SPO and CPO of amphibole is shown; note in italic the dominant deformation processes, see text for further details. wr: wall rock, hy: pre-strain hydration, sz: shear zone. Stage 0: Strong, anhydrous crust deformed in dislocation creep regime. Stage 1: Brittle failure drives localised fluid ingress and hydration reactions, weakening the crust. Stage 2: Further fluid input fully hydrates the crust and facilitates deformation in the dissolution–precipitation creep regime. Spatial dissipation of fluid along grain boundaries and subsequent reaction of dry wall rock widens the zone of hydrated and weak rock over time, while the fluid activity decreases. Subsequent brittle failure and fluid ingress events allow the shear zone to mature to the 100-m-wide structure that we observe today. The location of structural domains 1–4 and their respective dominant dyke fabric type (T0-3) is shown. (For interpretation of the references to colour in this figure legend, the reader is referred to the web version of this article.)

to dislocation creep, at equivalent P-T conditions (Marti et al., 2018; Malvoisin and Baumgartner, 2021; Lee et al., 2022; Mérit et al., 2025). In this way, where hydration is complete and sufficient fluid is uniformly available we expect the distribution of strain to be homogeneous. Where hydration is only local and partial, the distribution of strain will be heterogeneous.

5.4.3. Stage 2: Further fluid input fully hydrates the shear zone and facilitates deformation in the dissolution–precipitation creep regime

New fluid is not required for deformation to continue in the shear zone centre, provided the grain boundaries stay wetted. However, grain boundary fluid may deplete through the process of free water consumption via hydration reactions in the surrounding anhydrous wall rock (e.g. Moore et al., 2020). If this depletion results in a lack of sufficient fluid along the grain boundaries, deformation will cease and shear zone will 'harden'. In contrast, if deformation by dissolution–precipitation creep starts a feedback where ongoing deformation allows drawing in of more fluid (Fusseis et al., 2009; Menegon et al., 2015), then availability of fluid in the shear zone will increase and facilitate shear zone widening. Does quartz only precipitate as veins where the rock is fluid-saturated? This could explain why quartz veins are only observed in completely hydrated rock (where no clinopyroxene remains), and are apparently absent in undeformed T0 areas bearing clinopyroxene (Fig. 4c & d).

The finite width of the shear zone suggests that a finite reservoir of fluid was available. Externally introduced fluid would likely dissipate with time, producing a transient effect. Repeated fracture and fluid infiltration events allow the hydrated region of shear zone to widen, with fluid permeating out and reacting with the surrounding wall rock ahead of the deformation zone as the shear zone evolves (Stage 2, Fig. 14; i.e. Moore et al. 2020, 2024). In summary, local fluid influx triggers activation of low stress dissolution–precipitation creep and localised strain.

5.5. Wider rheological implications

5.5.1. Similar bulk strain rate in quartzofeldspathic gneiss and mafic dyke

Both the gneiss and dyke exhibit the same planar fabric and lineation in domains 3 and 4 (Fig. 3a & b), and the dyke-gneiss contact is planar (Fig. 3b i), which suggests both lithologies have a similar bulk rheology. The absence of undulatory fabric or pinch and swell structures at the contact between the two lithologies implies there is no significant rheological contrast (Fig. 3b i; Gardner et al. 2017b). This means for dissolution–precipitation creep, we expect the gneiss and dyke to behave very similarly, in agreement with field observations and laboratory experiments that find wet amphibolite exhibits a similar rheology to wet anorthite, at lower-crustal conditions (Getsinger et al., 2013; Getsinger and Hirth, 2014). A previous study of Lewisian Gneiss Complex amphibolite-facies metamorphism and deformation concludes that the mafic dykes are weaker than the surrounding gneisses, based on pre-deformation metamorphic reactions that reduce grain size (Pearce et al., 2011). During early deformation of the Upper Badcall shear zone it is possible that this holds true, as the overall grain size is larger in the gneiss than the dyke in domains 1 and 2 (Figs. 9b & 10b). However, once the shear zone and deformation fabrics are evolved (e.g. domains 3 and 4) then the grain size is similar for both the gneiss and the dyke and this could explain their apparently similar rheology (Figs. 9b & 10b).

5.5.2. Localised activation of 'Newtonian' dissolution–precipitation creep as a trigger for strain localisation – a special case or not?

In the absence of other factors, Newtonian behaviour alone cannot localise deformation. Hence, for such a process to be important in the localisation of strain then additional processes must occur. As outlined above, we suggest that a local introduction and availability of fluid determines where strain localises through the activation of deformation by dissolution–precipitation creep, which is weaker than dislocation creep at equivalent P-T conditions provided sufficient fluid is available (Marti et al., 2018; Malvoisin and Baumgartner, 2021; Lee et al., 2022; Mérit et al., 2025).

A growing body of literature attributes strain localisation to dissolution–precipitation creep in a number of cm- to m-scale mid-crustal shear zones (Menegon et al., 2008; Lee et al., 2022; Moore et al., 2020, 2024; Mérit et al., 2025), and identifies dissolution–precipitation creep as a significant process within km-scale shear zones and deformed units (Wintsch and Yi, 2002; Díaz Aspiroz et al., 2007; Stokes et al., 2012; Giuntoli et al., 2018; Trepmann and Seybold, 2019; Wintsch et al., 2024). Our study provides insight into the localised initiation and evolution of strain within a large-scale mid-crustal shear zone that deforms by dissolution–precipitation creep, and contributes to our understanding of how fluid-rock interaction can promote crustal weakening.

We question whether signatures of dissolution–precipitation creep have been overlooked or misinterpreted as annealed in some cases, due to the subtle signatures it produces in rocks: a lack of intra-grain deformation (crystal-plasticity) and relatively large grain size relative to typical mylonites produced by dynamic grain size reduction. The non-genetic definition of such deformed rocks would be blastomylonites: cohesive, foliated fault rocks with pronounced grain growth (Sibson, 1977; Woodcock and Mort, 2008); however, this definition means blastomylonites are invariably associated with annealing processes. In our study, the nature of matrix formation in the shear zone is by grain size refinement (grain size reduction or increase depending on the starting grain size and chemistry), and overall grain size increase in the dyke (amphibole and quartz) and gneiss (Figs. 9 & 10). Grain size increase is in this case consistent with numerical models that demonstrate grain growth with deformation (Bons and Den Brok, 2000; Piazolo et al., 2002) and observations from elsewhere in the Lewisian Gneiss Complex (Beach, 1974a; Pearce et al., 2011). Related to the potential misinterpretation of the signatures produced in rocks by dissolution–precipitation creep is the fact that dissolution–precipitation creep can produce CPO of elastically anisotropic minerals such as amphibole and phyllosilicates (Kamb, 1959; Bons and Den Brok, 2000; Wenk et al., 2020). This means that areas of the crust interpreted to deform by dislocation creep based on their seismic anisotropy, may in fact deform by dissolution–precipitation creep if a significant proportion of anisotropic minerals are present.

The Upper Badcall shear zone is one of many 1–100 m discrete, steeply dipping shear zones across the Assynt terrane and, together with larger structures such as the Laxford and Canisp shear zone, are estimated to be responsible for 22.5 km of horizontal displacement in total (Fig. 1a; Beach 1974a,b, Goodenough et al. 2010). If processes in the Upper Badcall shear zone are equivalent to processes in the shear zone population as a whole, then dissolution–precipitation creep can be attributed to accommodating a significant amount of deformation. Similar signatures of dissolution–precipitation creep have been identified in km-scale mid- to lower-crustal shear zones and uniformly deformed units (Wintsch and Yi, 2002; Díaz Aspiroz et al., 2007; Stokes et al., 2012; Giuntoli et al., 2018; Trepmann and Seybold, 2019; Wintsch et al., 2024). We suggest that greater recognition and characterisation of such processes, where applicable according to geological history and setting, is required to ensure that geophysical models of crustal deformation accurately represent natural processes.

Finally, dissolution–precipitation creep facilitated by fluid infiltration offers a mechanism that can produce transient rheology in the mid-crust, as identified in geophysical data (Ingleby and Wright, 2017; Hussain et al., 2018; Weiss et al., 2019; Tian et al., 2020), as a weakening response to discrete fluid input followed by gradual strengthening through dissipation of that fluid through reaction and spatial migration. Further work is needed to understand how this transient fluid-reaction-deformation cycle influences large-scale deformation of the continental crust, and to align geological knowledge of flow laws with geophysical observations and models. Laboratory experiments that can capture the process of dissolution–precipitation creep across a range of lithology, deformation and P-T conditions would greatly aid the implementation of this process into rheological models.

6. Conclusions

Our field-based microstructural and minerochemical study shows how localised introduction of fluid facilitates strain localisation through activation of spatially-confined dissolution–precipitation creep, to produce the 100-m-wide mid-crustal Upper Badcall shear zone. To determine the deformation process, we analyse representative areas of both mafic dyke and quartzofeldspathic gneiss at map, outcrop and thin section scale, in a transect from 1 km away in the wall rock to the shear zone centre.

Signatures of dissolution–precipitation creep identified in this shear zone include strong CPO development of amphibole contrasted by weak to absent CPO for quartz and plagioclase, and strong SPO in amphibole, plagioclase and quartz. We also observe indented, asymmetrically truncated grains, and grains with preferentially grown chemically distinct asymmetric rims and/or elongate tails. Within amphibole or biotite-dominant areas, grain boundaries align to form planar surfaces that extend over several grains, potentially as 'weak sliding surfaces'. In the

highest strain domain the microstructure, grain-chemistry and strain distribution is relatively 'homogeneous' and grain size is near unimodal. Overall, grain size increases slightly from outside to inside the shear zone and there is a lack of signatures of crystal-plasticity, such as lattice bending, subgrains and core-mantle structures, in all mineral phases.

We propose a model of shear zone evolution that involves an interplay between several related processes: (1) spatially-confined influx of fluids infiltrate through small-scale fractures, (2) localised hydration reactions occur due to fluid influx, and (3) dominant deformation regime switches from dislocation creep to dissolution–precipitation creep where enough fluid is available for grain boundaries to be sufficiently wet. The shear zone widens as fluid progressively migrates into and hydrates the surrounding wall rock. This behaviour is interpreted to be transient as additional water influx is needed to keep grain boundaries wet during shear zone widening.

We suggest that signatures of dissolution–precipitation creep may be overlooked in the mid- to lower-crust, even though the activity of dissolution–precipitation creep has important rheological consequences for the deformation of the Earth's crust: (1) dissolution–precipitation creep weakens the crust relative to regions that deform by dislocation creep, (2) CPO development through dissolution–precipitation creep involving elastically anisotropic minerals will result in strong seismic anisotropy, (3) transient weakening of the mid- and lower-crust, as inferred from our study, may be important for the behaviour of faults throughout the seismic cycle, where mobilisation of fluids during earthquakes may temporarily promote dissolution–precipitation creep in the postseismic period.

Our work highlights the potential for dissolution–precipitation creep to be a transient process in shear zones; it is expected to be recognisable in geophysical data - either through seismological studies of shear zone structure, or geodetic studies of time-variable deformation processes associated with active faults.

CRediT authorship contribution statement

Manon Carpenter: Writing – review & editing, Writing – original draft, Visualization, Validation, Methodology, Investigation, Formal analysis, Data curation, Conceptualization. **Sandra Piazolo:** Writing – review & editing, Validation, Supervision, Resources, Project administration, Methodology, Funding acquisition, Conceptualization. **Tim Craig:** Writing – review & editing, Validation, Supervision, Resources, Project administration, Funding acquisition, Conceptualization. **Tim J. Wright:** Writing – review & editing, Validation, Supervision, Resources, Project administration, Funding acquisition, Conceptualization.

Declaration of competing interest

The authors declare that they have no known competing financial interests or personal relationships that could have appeared to influence the work reported in this paper.

Acknowledgements

The authors thank Jack McGrath and Giulia Fedrizzi for assistance in the field, and Harri Williams and Richard Walshaw at Leeds Electron Microscopy and Spectroscopy Centre for their respective assistance with rock preparation and microprobe analysis. The authors acknowledge the use of the FEI Quanta 650 SEM, Jeol 8230 microprobe and Tescan VEGA3 XM within the Leeds Electron Microscopy and Spectroscopy Centre, University of Leeds. We also thank NatureScot for confirming that our sampling procedure (minimal, discrete sampling using a geological hammer) proposed for this study was appropriate given the Geological Conservation Review status of the location. We thank Francesco Giuntoli and an anonymous reviewer for constructive reviews that have greatly improved this manuscript. This work was supported by the Leeds-York-Hull Natural Environment Research Council (NERC) Doctoral Training Partnership (DTP) Panorama under grant NE\S007458\1. Tim Craig thanks the Royal Society, United Kingdom for support under URF\R1\180088 and URF\R\231019. Tim Craig and Tim J Wright were also supported through COMET, which is the NERC Centre for the Observation and Modelling of Earthquakes, Volcanoes and Tectonics, a partnership between UK Universities and the British Geological Survey.

Appendix A. Supplementary data

Supplementary material related to this article can be found online at https://doi.org/10.1016/j.jsg.2025.105461.

Data availability

Data will be made available on request.

References

Attfield, P., 1987. The Structural History of the Canisp Shear Zone. Technical Report, pp. 165–173. http://dx.doi.org/10.1144/GSL.SP.1987.027.01.14, URL http://sp.lyellcollection.org/.

Beach, A., 1973. The mineralogy of high temperature shear zones at Scourie, NW Scotland. J. Petrol. 14 (2), 231–248.

Beach, A., 1974a. Amphibolitization of Scourian granulites. Scott. J. Geol. 10 (1), 35–43.

Beach, A., 1974b. The measurement and significance of displacements on Laxfordian Shear Zones, North-West Scotland. Proc. the Geologists' Assoc. 85 (1), 13–IN1. http://dx.doi.org/10.1016/S0016-7878(74)80032-5.

Beach, A., 1980. Retrogressive metamorphic processes in shear zones with special reference to the Lewisian complex. J. Struct. Geol. 2 (1–2), 257–263. http://dx.doi.org/10.1016/0191-8141(80)90058-9.

Beach, A., Coward, M.P., Graham, R.H., 1974. An interpretation of the structural evolution of the Laxford Front, north-west Scotland. Scott. J. Geol. 9 (4), 297–308. http://dx.doi.org/10.1144/sjg09040297.

Boland, J.N., Tullis, T.E., 1986. Deformation behavior of wet and dry clinopyroxenite in the brittle to ductile transition region. Miner. Rock Deform.: Lab. Stud. 36, 35–49.

Bons, P.D., Den Brok, B., 2000. Crystallographic preferred orientation development by dissolution–precipitation creep. J. Struct. Geol. 22 (11–12), 1713–1722. http://dx.doi.org/10.1016/S0191-8141(00)00075-4.

Bons, P.D., Elburg, M.A., Gomez-Rivas, E., 2012. A review of the formation of tectonic veins and their microstructures. J. Struct. Geol. 43, 33–62.

Brander, L., Svahnberg, H., Piazolo, S., 2012. Brittle-plastic deformation in initially dry rocks at fluid-present conditions: Transient behaviour of feldspar at mid-crustal levels. Contrib. Miner. Pet. 163 (3), 403–425. http://dx.doi.org/10.1007/s00410-011-0677-5.

Bras, E., Baïsset, M., Yamato, P., Labrousse, L., 2021. Transient weakening during the granulite to eclogite transformation within hydrous shear zones (Holsnøy, Norway). Tectonophysics 819, http://dx.doi.org/10.1016/j.tecto.2021.229026.

Bürgmann, R., Dresen, G., 2008. Rheology of the lower crust and upper mantle: Evidence from rock mechanics, geodesy, and field observations. Annu. Rev. Earth Planet. Sci. 36, 531–567. http://dx.doi.org/10.1146/annurev.earth.36.031207.124326.

Carreras, J., 2001. Zooming on Northern Cap de Creus shear zones. J. Struct. Geol. 23 (9), 1457–1486. http://dx.doi.org/10.1016/S0191-8141(01)00011-6.

Carreras, J., Casas, J.M., 1987. On folding and shear zone-development: a mesoscale structural study on the transition between two different tectonic styles. Tectonophysics 135 (1–3), 87–98. http://dx.doi.org/10.1016/0040-1951(87)90154-5.

Carter, N.L., Horseman, S.T., Russell, J.E., Handin, J., 1993. Rheology of rocksalt. J. Struct. Geol. 15 (9–10), 1257–1271. http://dx.doi.org/10.1016/0191-8141(93)90168-A.

Cartwright, I., 1990. Prograde metamorphism, anatexis, and retrogression of the Scourian complex, north-west Scotland. In: High-Temperature Metamorphism and Crustal Anatexis. Springer, pp. 371–399.

Cartwright, I., Barnicoat, A.C., 1987. Petrology of Scourian supracrustal rocks and orthogneisses from Stoer, NW Scotland: implications for the geological evolution of the Lewisian complex. Geol. Soc. Lond. Spec. Publ. 27 (1), 93–107. http://dx.doi.org/10.1144/GSL.SP.1987.027.01.09.

Chapman, H.J., Moorbath, S., 1977. Lead isotope measurements from the oldest recognised Lewisian gneisses of north-west Scotland. Nature 268 (5615), 41–42.

Clerc, C., Jolivet, L., Ringenbach, J.C., 2015. Ductile extensional shear zones in the lower crust of a passive margin. Earth Planet. Sci. Lett. 431, 1–7. http://dx.doi.org/10.1016/J.EPSL.2015.08.038.

Cohen, A.S., O'Nions, R.K., O'Hara, M.J., 1991. Chronology and mechanism of depletion in Lewisian granulites. Contrib. Miner. Pet. 106, 142–153.
Corfu, F., Heaman, L.M., Rogers, G., 1994. Polymetamorphic evolution of the Lewisian complex, NW Scotland, as recorded by U-Pb isotopic compositions of zircon, titanite and rutile. Contrib. Miner. Pet. 117 (3), 215–228. http://dx.doi.org/10.1007/BF00310864.
Corvò, S., Maino, M., Langone, A., Schenker, F.L., Piazolo, S., Casini, L., Seno, S., 2021. Local variations of metamorphic record from compositionally heterogeneous rocks (Cima di Gagnone, Central Alps): Inferences on exhumation processes of (U)HP–HT rocks. Lithos 390–391, 106126. http://dx.doi.org/10.1016/J.LITHOS.2021.106126.
Corvò, S., Maino, M., Piazolo, S., Seno, S., Langone, A., 2022. Role of inherited compositional and structural heterogeneity in shear zone development at mid-low levels of the continental crust (the Anzola shear zone; Ivrea-Verbano Zone, Southern Alps). Lithos 422–423, 106745. http://dx.doi.org/10.1016/J.LITHOS.2022.106745.
Coward, M.P., Potts, G.J., 1983. Complex strain patterns developed at the frontal and lateral tips to shear zones and thrust zones. J. Struct. Geol. 5 (3), 383–399. http://dx.doi.org/10.1016/0191-8141(83)90025-1, URL https://www.sciencedirect.com/science/article/pii/0191814183900251.
Cross, A.J., Skemer, P., 2019. Rates of dynamic recrystallization in geologic materials. J. Geophys. Res.: Solid Earth 124 (2), 1324–1342. http://dx.doi.org/10.1029/2018JB016201.
Czaplińska, D., Piazolo, S., Zibra, I., 2015. The influence of phase and grain size distribution on the dynamics of strain localization in polymineralic rocks. J. Struct. Geol. 72, 15–32. http://dx.doi.org/10.1016/J.JSG.2015.01.001.
Dell'Angelo, L.N., Tullis, J., 1996. Textural and mechanical evolution with progressive strain in experimentally deformed aplite. Tectonophysics 256 (1–4), 57–82. http://dx.doi.org/10.1016/0040-1951(95)00166-2.
Díaz Aspiroz, M., Lloyd, G.E., Fernández, C., 2007. Development of lattice preferred orientation in clinoamphiboles deformed under low-pressure metamorphic conditions. A SEM/EBSD study of metabasites from the Aracena metamorphic belt (SW Spain). J. Struct. Geol. 29 (4), 629–645. http://dx.doi.org/10.1016/j.jsg.2006.10.010.
Droop, G., Fernandes, L., Shaw, S., 1999. Laxfordian metamorphic conditions of the Palaeoproterozoic Loch Maree Group, Lewisian Complex, NW Scotland. Scott. J. Geol. 35 (1), 31–50.
Drury, M.R., 2005. Dynamic recrystallization and strain softening of olivine aggregates in the laboratory and the lithosphere Rheology of olivine aggregates in the laboratory Low-strain rheology. Geol. Soc. Spec. Publ. 243 (1), 143–158. http://dx.doi.org/10.1144/GSL.SP.2005.243.01.11.
Evans, C.R., 1965. Geochronology of the Lewisian basement near Lochinver, Sutherland. Nature 207 (4992), 54–56.
Fagereng, A., Diener, J.F., Meneghini, F., Harris, C., Kvadsheim, A., 2018. Quartz vein formation by local dehydration embrittlement along the deep, tremorgenic subduction thrust interface. Geology 46 (1), 67–70. http://dx.doi.org/10.1130/G39649.1.
Fagereng, A., Diener, J.F.A., Tulley, C.J., Manda, B., 2024. Metamorphic inheritance, lower-crustal earthquakes, and continental rifting. Geochem. Geophys. Geosyst. 25 (3), e2023GC011305.
Fossen, H., Cavalcante, G.C.G., 2017. Shear zones – A review. Earth-Sci. Rev. 171, 434–455. http://dx.doi.org/10.1016/J.EARSCIREV.2017.05.002.
Friend, C.R.L., Kinny, P.D., 1995. New evidence for protolith ages of Lewisian granulites, northwest Scotland. Geology 23 (11), 1027–1030.
Friend, C., Kinny, P., 2001. A reappraisal of the Lewisian Gneiss Complex: geochronological evidence for its tectonic assembly from disparate terranes in the Proterozoic. Contrib. Miner. Pet. 142 (2), 198–218.
Fusseis, F., Regenauer-Lieb, K., Liu, J., Hough, R.M., De Carlo, F., 2009. Creep cavitation can establish a dynamic granular fluid pump in ductile shear zones. Nature 459 (7249), 974–977. http://dx.doi.org/10.1038/nature08051.
Gardner, R.L., Piazolo, S., Daczko, N.R., 2017b. Determining relative bulk viscosity of kilometre-scale crustal units using field observations and numerical modelling. Tectonophys. 721, 275–291. http://dx.doi.org/10.1016/j.tecto.2017.10.008.
Gardner, R., Piazolo, S., Evans, L., Daczko, N., 2017a. Patterns of strain localization in heterogeneous, polycrystalline rocks – a numerical perspective. Earth Planet. Sci. Lett. 463, 253–265. http://dx.doi.org/10.1016/J.EPSL.2017.01.039.
Gardner, J., Wheeler, J., 2021. The influence of large second phase grains on microstructural evolution during diffusion creep. J. Struct. Geol. 148, http://dx.doi.org/10.1016/j.jsg.2021.104371.
Gerbi, C., Johnson, S.E., Shulman, D., Klepeis, K., 2016. Influence of microscale weak zones on bulk strength. Geochem. Geophys. Geosyst. 17 (10), 4064–4077.
Getsinger, A.J., Hirth, G., 2014. Amphibole fabric formation during diffusion creep and the rheology of shear zones. Geology 42 (6), 535–538. http://dx.doi.org/10.1130/G35327.1.
Getsinger, A.J., Hirth, G., Stünitz, H., Goergen, E.T., 2013. Influence of water on rheology and strain localization in the lower continental crust. Geochem. Geophys. Geosyst. 14 (7), 2247–2264. http://dx.doi.org/10.1002/ggge.20148.
Giuntoli, F., Menegon, L., Warren, C.J., 2018. Replacement reactions and deformation by dissolution and precipitation processes in amphibolites. J. Metamorph. Geol. 36 (9), 1263–1286. http://dx.doi.org/10.1111/jmg.12445.
Giuntoli, F., Viola, G., Sørensen, B.E., 2022. Deformation mechanisms of blueschist facies continental metasediments may offer insights into deep episodic tremor and slow slip events. J. Geophys. Res.: Solid Earth 127 (10), e2022JB024265.
Goddard, R.M., Hansen, L.N., Wallis, D., Stipp, M., Holyoke, III, C.W., Kumamoto, K.M., Kohlstedt, D.L., 2020. A subgrain-size piezometer calibrated for EBSD. Geophys. Res. Lett. 47 (23), e2020GL090056.
Gomez-Rivas, E., Butler, R.W., Healy, D., Alsop, I., 2020. From hot to cold - The temperature dependence on rock deformation processes: An introduction. J. Struct. Geol. 132, 103977. http://dx.doi.org/10.1016/J.JSG.2020.103977.
Goodenough, K.M., Crowley, Q.G., Krabbendam, M., Parry, S.F., 2013. New U-Pb age constraints for the Laxford Shear Zone, NW Scotland: Evidence for tectono-magmatic processes associated with the formation of a Paleoproterozoic supercontinent. Precambrian Res. 233, 1–19. http://dx.doi.org/10.1016/j.precamres.2013.04.010.
Goodenough, K.M., Park, R.G., Krabbendam, M., Myers, J.S., Wheeler, J., Loughlin, S.C., Crowley, Q.G., Friend, C.R., Beach, A., Kinny, P.D., Graham, R.H., 2010. The Laxford shear zone: An end-Archaean terrane boundary? Geol. Soc. Spec. Publ. 335, 103–120. http://dx.doi.org/10.1144/SP335.6.
Gottardi, R., Mire, C., Davis, N., Casale, G., 2024. Effect of water-rock ratio on the stable isotope record of fluid-rock-deformation interactions in detachment shear zone. Geochem. Geophys. Geosyst. 25 (5), http://dx.doi.org/10.1029/2023GC011340, e2023GC011340.
Gratier, J.P., 1987. Pressure solution-deposition creep and associated tectonic differentiation in sedimentary rocks. Geol. Soc. Lond. Spec. Publ. 29 (1), 25–38.
Gratier, J.P., Dysthe, D.K., Renard, F., 2013. The role of pressure solution creep in the ductility of the earth's upper crust. In: Advances in Geophysics, vol. 54, Academic Press Inc., pp. 47–179. http://dx.doi.org/10.1016/B978-0-12-380940-7.00002-0.
Grund, S., John, T., Vrijmoed, J.C., Austrheim, H., Andersen, T.B., 2025. A mechanistic look at the amphibolitization of mafic crust: Insights from the Kråkeneset Gabbro body, Western Gneiss Region, Norway. J. Metamorph. Geol. 43 (4), 385–405. http://dx.doi.org/10.1111/jmg.12809.
Halfpenny, A., Prior, D.J., Wheeler, J., 2006. Analysis of dynamic recrystallization and nucleation in a quartzite mylonite. Tectonophysics 427 (1–4), 3–14. http://dx.doi.org/10.1016/J.TECTO.2006.05.016.
Hamilton, P.J., Evensen, N.M., O'nions, R.K., Tarney, J., 1979. Sm—Nd systematics of Lewisian gneisses: implications for the origin of granulites. Nature 277 (5691), 25–28.
Handy, M.R., 1994. Flow laws for rocks containing two non-linear viscous phases: a phenomenological approach. J. Struct. Geol. 16 (3), 287–301.
Hayman, N.W., Lavier, L.L., 2014. The geologic record of deep episodic tremor and slip. Geology 42 (3), 195–198. http://dx.doi.org/10.1130/G34990.1.
Henstock, T.J., Levander, A., Hole, J.A., 1997. Deformation in the lower crust of the San Andreas fault system in northern California. Science 278 (5338), 650–653.
Hirth, G., Kohlstedt, D., 2003. Rheology of the upper mantle and the mantle wedge: A view from the experimentalists. In: Geophysical Monograph-American Geophysical Union, vol. 138, AGU American Geophysical Union, pp. 83–106.
Hirth, G., Tullis, J., 1994. The brittle-plastic transition in experimentally deformed quartz aggregates. J. Geophys. Res.: Solid Earth 99 (B6), 11731–11747.
Holdsworth, R.E., Selby, D., Dempsey, E., Scott, L., Hardman, K., Fallick, A.E., Bullock, R., 2020. The nature and age of Mesoproterozoic strike-slip faulting based on Re–Os geochronology of syntectonic copper mineralization, Assynt Terrane, NW Scotland. J. Geol. Soc. 177 (4), 686–699.
Hussain, E., Wright, T.J., Walters, R.J., Bekaert, D.P., Lloyd, R., Hooper, A., 2018. Constant strain accumulation rate between major earthquakes on the North Anatolian Fault. Nat. Commun. 9 (1), http://dx.doi.org/10.1038/s41467-018-03739-2.
Ingleby, T., Wright, T.J., 2017. Omori-like decay of postseismic velocities following continental earthquakes. Geophys. Res. Lett. 44 (7), 3119–3130. http://dx.doi.org/10.1002/2017GL072865.
Ingles, J., Lamouroux, C., Soula, J.C., Guerrero, N., Debat, P., 1999. Nucleation of ductile shear zones in a granodiorite under greenschist facies conditions, Néouvielle massif, Pyrenees, France. J. Struct. Geol. 21 (5), 555–576. http://dx.doi.org/10.1016/S0191-8141(99)00042-5.
Kamb, W.B., 1959. Theory of preferred crystal orientation developed by crystallization under stress. J. Geol. 67 (2), 153–170. http://dx.doi.org/10.1086/626571.
Karato, S.i., Wu, P., 1993. Rheology of the upper mantle: A synthesis. Sci. (Am. Assoc. Adv. Sci.) 260 (5109), 771–778. http://dx.doi.org/10.1126/science.260.5109.771.
Kaufmann, G., Amelung, F., 2000. Reservoir-induced deformation and continental rheology in vicinity of Lake Mead, Nevada. J. Geophys. Res. 105 (B7), 16341–16358. http://dx.doi.org/10.1029/2000JB900079.
Kenner, S.J., Segall, P., 2003. Lower crustal structure in northern California: Implications from strain rate variations following the 1906 San Francisco earthquake. J. Geophys. Res. 108 (B1), http://dx.doi.org/10.1029/2001JB000189, 5–1.
Kinny, P.D., Friend, C.R.L., 1997. U-Pb isotopic evidence for the accretion of different crustal blocks to form the Lewisian Complex of northwest Scotland. Contrib. Miner. Pet. 129 (4), 326–340. http://dx.doi.org/10.1007/s004100050340.
Kinny, P.D., Friend, C.R.L., Love, G.J., 2005. Proposal for a terrane-based nomenclature for the Lewisian gneiss complex of NW Scotland. J. Geol. Soc. 162 (1), 175–186. http://dx.doi.org/10.1144/0016-764903-149.
Kirby, S.H., 1985. Rock mechanics observations pertinent to the rheology of the continental lithosphere and the localization of strain along shear zones. Tectonophysics 119 (1), 1–27. http://dx.doi.org/10.1016/0040-1951(85)90030-7.
Knipe, R.J., 1989. Deformation mechanisms — recognition from natural tectonites. J. Struct. Geol. 11 (1), 127–146. http://dx.doi.org/10.1016/0191-8141(89)90039-4.

Kruse, R., Stünitz, H., 1999. Deformation mechanisms and phase distribution in mafic high-temperature mylonites from the Jotun Nappe, southern Norway. Tectonophysics 303 (1), 223–249. http://dx.doi.org/10.1016/S0040-1951(98)00255-8.

Lee, A.L., Stünitz, H., Soret, M., Battisti, M.A., 2022. Dissolution precipitation creep as a process for the strain localisation in mafic rocks. J. Struct. Geol. 155, http://dx.doi.org/10.1016/j.jsg.2021.104505.

Lusk, A.D., Platt, J.P., 2020. The deep structure and rheology of a plate boundary-scale shear zone: Constraints from an Exhumed Caledonian Shear Zone, NW Scotland. Lithosphere 2020 (1), 1–33. http://dx.doi.org/10.2113/2020/8824736.

Malvoisin, B., Baumgartner, L.P., 2021. Mineral Dissolution and Precipitation Under Stress: Model Formulation and Application to Metamorphic Reactions. Geochem. Geophys. Geosyst. 22 (5), http://dx.doi.org/10.1029/2021GC009633.

Mandal, N., Kumar Samanta, S., Chakraborty, C., 2004. Problem of folding in ductile shear zones: a theoretical and experimental investigation. J. Struct. Geol. 26 (3), 475–489. http://dx.doi.org/10.1016/j.jsg.2003.07.004.

Mansard, N., Stünitz, H., Raimbourg, H., Précigout, J., 2020. The role of deformation-reaction interactions to localize strain in polymineralic rocks: Insights from experimentally deformed plagioclase-pyroxene assemblages. J. Struct. Geol. 134, http://dx.doi.org/10.1016/j.jsg.2020.104008.

Marti, S., Stünitz, H., Heilbronner, R., Plümper, O., Kilian, R., 2018. Syn-kinematic hydration reactions, grain size reduction, and dissolution-precipitation creep in experimentally deformed plagioclase-pyroxene mixtures. Solid Earth 9 (4), 985–1009. http://dx.doi.org/10.5194/se-9-985-2018.

McCaig, A., 1988. Deep fluid circulation in fault zones. Geol. 16 (10), 867. http://dx.doi.org/10.1130/0091-7613(1988)016<0867:DFCIFZ>2.3.CO;2.

McNamara, D.D., Wheeler, J., Pearce, M., Prior, D.J., 2012. Fabrics produced mimetically during static metamorphism in retrogressed eclogites from the Zermatt-Saas zone, Western Italian Alps. J. Struct. Geol. 44, 167–178.

McNamara, D.D., Wheeler, J., Pearce, M., Prior, D.J., 2024. A key role for diffusion creep in eclogites: Omphacite deformation in the Zermatt-Saas unit, Italian Alps. J. Struct. Geol. 179, http://dx.doi.org/10.1016/j.jsg.2023.105033.

Menegon, L., Fusseis, F., Stünitz, H., Xiao, X., 2015. Creep cavitation bands control porosity and fluid flow in lower crustal shear zones. Geol. 43 (3), 227–230. http://dx.doi.org/10.1130/G36307.1.

Menegon, L., Pennacchioni, G., Spiess, R., 2008. Dissolution-precipitation creep of K-feldspar in mid-crustal granite mylonites. J. Struct. Geol. 30 (5), 565–579. http://dx.doi.org/10.1016/j.jsg.2008.02.001.

Mérit, L., Soret, M., Dubacq, B., Agard, P., Précigout, J., Stünitz, H., 2025. Grain-scale feedback between deformation mechanisms and metamorphic reactions: Dissolution-precipitation processes in the lower crust (Kågen gabbros). Earth Planet. Sci. Lett. 656, http://dx.doi.org/10.1016/j.epsl.2025.119275.

Mongkoltip, P., Ashworth, J.R., 1983. Exsolution of ilmenite and rutile in hornblende. Am. Miner. 68 (1–2), 143–155.

Moorbath, S., Welke, H., Gale, N.H., 1969. The significance of lead isotope studies in ancient, high-grade metamorphic basement complexes, as exemplified by the Lewisian rocks of northwest Scotland. Earth Planet. Sci. Lett. 6 (4), 245–256.

Moore, J., Beinlich, A., Piazolo, S., Austrheim, H., Putnis, A., 2020. Metamorphic differentiation via enhanced dissolution along high permeability zones. J. Petrol. 61 (10), http://dx.doi.org/10.1093/petrology/egaa096.

Moore, J., Piazolo, S., Beinlich, A., Austrheim, H., Putnis, A., 2024. Brittle initiation of dissolution–precipitation creep in plagioclase-rich rocks: insights from the Bergen arcs, Norway. Contrib. Miner. Pet. 179 (6), http://dx.doi.org/10.1007/s00410-024-02141-0.

Orlandini, O.F., Mahan, K.H., 2020. Rheological evolution of a pseudotachylyte-bearing deep crustal shear zone in the western Canadian shield. J. Struct. Geol. 141, http://dx.doi.org/10.1016/j.jsg.2020.104188.

Park, R.G., 1970. Observations on Lewisian chronology. Scott. J. Geol. 6 (4), 379–399.

Park, R.G., Tarney, J., 1987. The Lewisian complex: a typical Precambrian high-grade terrain? In: Evolution of the Lewisian and Comparable Precambrian High Grade Terrains, vol. 27, (1), The Geological Society of London, pp. 13–25. http://dx.doi.org/10.1144/GSL.SP.1987.027.01.03.

Passchier, C., Trouw, R., 2005. Microtectonics. Scholars Portal.

Peach, B.N., 1907. The Geological Structure of the North-West Highlands of Scotland. HM Stationery Office.

Pearce, M.A., Wheeler, J., 2014. Microstructural and metamorphic constraints on the thermal evolution of the southern region of the Lewisian Gneiss Complex, NW Scotland. J. Petrol. 55 (10), 2043–2066. http://dx.doi.org/10.1093/petrology/egu049.

Pearce, M.A., Wheeler, J., Prior, D.J., 2011. Relative strength of mafic and felsic rocks during amphibolite facies metamorphism and deformation. J. Struct. Geol. 33 (4), 662–675. http://dx.doi.org/10.1016/j.jsg.2011.01.002.

Pennacchioni, G., Mancktelow, N.S., 2007. Nucleation and initial growth of a shear zone network within compositionally and structurally heterogeneous granitoids under amphibolite facies conditions. J. Struct. Geol. 29 (11), 1757–1780. http://dx.doi.org/10.1016/j.jsg.2007.06.002.

Piazolo, S., Bons, P.D., Jessell, M.W., Evans, L., Passchier, C.W., 2002. Dominance of microstructural processes and their effect on microstructural development: insights from numerical modelling of dynamic recrystallization. In: Deformation Mechanisms, Rheology and Tectonics: Current Status and Future Perspectives, vol. 200, (1), The Geological Society of London, pp. 149–170. http://dx.doi.org/10.1144/GSL.SP.2001.200.01.10.

Piazolo, S., Passchier, C.W., 2002. Controls on lineation development in low to medium grade shear zones: a study from the Cap de Creus peninsula, NE Spain. J. Struct. Geol. 24 (1), 25–44. http://dx.doi.org/10.1016/S0191-8141(01)00045-1.

Platt, J.P., Behr, W.M., Cooper, F.J., 2015. Metamorphic core complexes; windows into the mechanics and rheology of the crust. J. Geol. Soc. 172 (1), 9–27. http://dx.doi.org/10.1144/jgs2014-036.

Prior, D.J., Wheeler, J., Peruzzo, L., Spiess, R., Storey, C., 2002. Some garnet microstructures: an illustration of the potential of orientation maps and misorientation analysis in microstructural studies. J. Struct. Geol. 24 (6), 999–1011. http://dx.doi.org/10.1016/S0191-8141(01)00087-6.

Putnis, A., 2009. Mineral replacement reactions. Rev. Mineral. Geochem. 70 (1), 87–124. http://dx.doi.org/10.2138/rmg.2009.70.3.

Putnis, A., 2021. Fluid-mineral interactions: Controlling coupled mechanisms of reaction, mass transfer and deformation. J. Petrol. 62 (12), http://dx.doi.org/10.1093/petrology/egab092.

Ramsay, J., 1980. Shear zone geometry: a review. J. Struct. Geol. 2 (1–2), 83–99.

Ramsay, J.G., Graham, R.H., 1970. Strain variation in shear belts. Can. J. Earth Sci. 7 (3), 786–813. http://dx.doi.org/10.1139/e70-078.

Rutter, E.H., 1976. A Discussion on natural strain and geological structure - The kinetics of rock deformation by pressure solution. Philos. Trans. R. Soc. Lond. Ser. A: Math. Phys. Sci. 283 (1312), 203–219. http://dx.doi.org/10.1098/rsta.1976.0079.

Rutter, E.H., Brodie, K.H., 1985. The permeation of water into hydrating shear zones. In: Thompson, A.B., Rubie, D.C. (Eds.), Metamorphic Reactions: Kinetics, Textures, and Deformation. Springer New York, New York, NY, pp. 242–250. http://dx.doi.org/10.1007/978-1-4612-5066-1-9.

Rutter, E.H., Brodie, K.H., 1988. The role of tectonic grain size reduction in the rheological stratification of the lithosphere. Geol. Rundsch. 77 (1), 295–307. http://dx.doi.org/10.1007/BF01848691.

Rutter, E.H., Holdsworth, R.E., Knipe, R.J., 2001. The nature and tectonic significance of fault-zone weakening: an introduction. Geol. Soc. Spec. Publ. 186 (1), 1–11. http://dx.doi.org/10.1144/GSL.SP.2001.186.01.01.

Rybacki, E., Dresen, G., 2000. Dislocation and diffusion creep of synthetic anorthite aggregates. J. Geophys. Res. 105 (B11), 26017–26036. http://dx.doi.org/10.1029/2000JB900223.

Schmid, S.M., Paterson, M.S., Boland, J.N., 1980. High temperature flow and dynamic recrystallization in carrara marble. Tectonophysics 65 (3), 245–280. http://dx.doi.org/10.1016/0040-1951(80)90077-3.

Segall, P., Simpson, C., 1986. Nucleation of ductile shear zones on dilatant fractures. Geol. (Boulder) 14 (1), 56–59. http://dx.doi.org/10.1130/0091-7613(1986)14<56:NODSZO>2.0.CO;2.

Shannon, R.D., Rossi, R.C., 1964. Definition of topotaxy. Nature 202 (4936), 1000–1001.

Sibson, R.H., 1977. Fault rocks and fault mechanisms. J. Geol. Soc. 133 (3), 191–213. http://dx.doi.org/10.1144/gsjgs.133.3.0191.

Sibson, R.H., 1981. Fluid flow accompanying faulting: field evidence and models. In: Earthquake Prediction: An International Review, vol. 4, Wiley Online Library, pp. 593–603.

Sibson, R.H., 1994. Crustal stress, faulting and fluid flow. Geol. Soc. Lond. Spec. Publ. 78 (1), 69–84.

Sills, J.D., 1982. The retrogression of ultramafic granulites from the Scourian of NW Scotland. Miner. Mag. 46 (338), 55–61.

Sills, J.D., Rollinson, H.R., 1987. Metamorphic evolution of the mainland Lewisian complex. Geol. Soc. Lond. Spec. Publ. 27 (1), 81–92. http://dx.doi.org/10.1144/GSL.SP.1987.027.01.08.

Smith, J.R., Piazolo, S., Daczko, N.R., Evans, L., 2015. The effect of pre-tectonic reaction and annealing extent on behaviour during subsequent deformation: insights from paired shear zones in the lower crust of Fiordland, New Zealand. J. Metamorph. Geol. 33 (6), 557–577. http://dx.doi.org/10.1111/jmg.12132.

Sorensen, K., 1983. Growth and dynamics of the Nordre Stromfjord shear zone. J. Geophys. Res. 88 (B4), 3419–3437. http://dx.doi.org/10.1029/JB088iB04p03419.

Soret, M., Agard, P., Ildefonse, B., Dubacq, B., Prigent, C., Rosenberg, C., 2019. Deformation mechanisms in mafic amphibolites and granulites: Record from the Semail metamorphic sole during subduction infancy. Solid Earth 10 (5), 1733–1755. http://dx.doi.org/10.5194/se-10-1733-2019.

Steffen, K., Selverstone, J., Brearley, A., 2001. Episodic weakening and strengthening during synmetamorphic deformation in a deep-crustal shear zone in the Alps. Geol. Soc. Lond. Spec. Publ. 186 (1), 141–156.

Stenvall, C.A., Fagereng, A., Diener, J.F., 2019. Weaker than weakest: On the strength of shear zones. Geophys. Res. Lett. 46 (13), 7404–7413. http://dx.doi.org/10.1029/2019GL083388.

Stenvall, C.A., Fagereng, A., Diener, J.F.A., Harris, C., Janney, P.E., 2020. Sources and effects of fluids in continental retrograde shear zones: Insights from the Kuckaus Mylonite Zone, Namibia. Geofluids 2020, 1–21. http://dx.doi.org/10.1155/2020/3023268.

Stipp, M., Stünitz, H., Heilbronner, R., Schmid, S.M., 2002. Dynamic recrystallization of quartz: correlation between natural and experimental conditions. In: Deformation Mechanisms, Rheology and Tectonics: Current Status and Future Perspectives, vol. 200, (1), The Geological Society of London, pp. 171–190. http://dx.doi.org/10.1144/GSL.SP.2001.200.01.11.

Stokes, M.R., Wintsch, R.P., Southworth, C.S., 2012. Deformation of amphibolites via dissolution-precipitation creep in the middle and lower crust. J. Metamorph. Geol. 30 (7), 723–737. http://dx.doi.org/10.1111/j.1525-1314.2012.00989.x.

Stuart, C.A., Meek, U., Daczko, N.R., Piazolo, S., Huang, J.X., 2018. Chemical signatures of melt-rock interaction in the root of a magmatic arc. J. Petrol. 59 (2), 321–340. http://dx.doi.org/10.1093/petrology/egy029.

Stünitz, H., Neufeld, K., Heilbronner, R., Finstad, A.K., Konopásek, J., Mackenzie, J.R., 2020. Transformation weakening: Diffusion creep in eclogites as a result of interaction of mineral reactions and deformation. J. Struct. Geol. 139, 104129.

Stünitz, H., Tullis, J., 2001. Weakening and strain localization produced by syn-deformational reaction of plagioclase. Int. J. Earth Sci. 90, 136–148.

Sutton, J., Watson, J., 1950. The pre-Torridonian metamorphic history of the Loch Torridon and Scourie areas in the North-West Highlands, and its bearing on the chronological classification of the Lewisian. Q. J. Geol. Soc. Lond. 106 (1–4), 241–307. http://dx.doi.org/10.1144/GSL.JGS.1950.106.01-04.16.

Svahnberg, H., Piazolo, S., 2010. The initiation of strain localisation in plagioclase-rich rocks: Insights from detailed microstructural analyses. J. Struct. Geol. 32 (10), 1404–1416. http://dx.doi.org/10.1016/j.jsg.2010.06.011.

Takeuchi, C.S., Fialko, Y., 2012. Dynamic models of interseismic deformation and stress transfer from plate motion to continental transform faults. J. Geophys. Res.: Solid Earth 117 (B5), http://dx.doi.org/10.1029/2011JB009056.

Tarney, J., 1963. Assynt dykes and their metamorphism. Nature 199 (4894), 672–674.

Tatham, D.J., Casey, M., 2007. Inferences from shear zone geometry: an example from the Laxfordian shear zone at Upper Badcall, Lewisian Complex, NW Scotland. In: Deformation of the Continental Crust: The Legacy of Mike Coward, vol. 272, (1), The Geological Society of London, pp. 47–57. http://dx.doi.org/10.1144/GSL.SP.2007.272.01.04.

Teall, J.J.H., 1885. The Metamorphosis of Dolerite into Hornblende-schist. Q. J. Geol. Soc. Lond. 41 (1–4), 133–145. http://dx.doi.org/10.1144/GSL.JGS.1885.041.01-04.19.

Tian, Z., Freymueller, J.T., Yang, Z., 2020. Spatio-temporal variations of afterslip and viscoelastic relaxation following the Mw 7.8 Gorkha (Nepal) earthquake. Earth Planet. Sci. Lett. 532, 116031. http://dx.doi.org/10.1016/J.EPSL.2019.116031.

Tokle, L., Hirth, G., 2021. Assessment of Quartz Grain Growth and the Application of the Wattmeter to Predict Quartz Recrystallized Grain Sizes. J. Geophys. Res. Solid Earth 126 (7), n/a. http://dx.doi.org/10.1029/2020JB021475.

Trepmann, C.A., Seybold, L., 2019. Deformation at low and high stress-loading rates. Geosci. Front. 10 (1), 43–54. http://dx.doi.org/10.1016/j.gsf.2018.05.002, URL https://www.sciencedirect.com/science/article/pii/S167498711830104X.

Trimby, P.W., Prior, D.J., Wheeler, J., 1998. Grain boundary hierarchy development in a quartz mylonite. J. Struct. Geol. 20 (7), 917–935. http://dx.doi.org/10.1016/S0191-8141(98)00026-1.

Twiss, R.J., 1977. Theory and applicability of a recrystallized grain size paleopiezometer. Pure Appl. Geophys. 115 (1–2), 227–244. http://dx.doi.org/10.1007/BF01637105.

Viegas, G., Menegon, L., Archanjo, C., 2016. Brittle grain-size reduction of feldspar, phase mixing and strain localization in granitoids at mid-crustal conditions (Pernambuco shear zone, NE Brazil). Solid Earth (Göttingen) 7 (2), 375–396. http://dx.doi.org/10.5194/se-7-375-2016.

Warren, J.M., Hirth, G., 2006. Grain size sensitive deformation mechanisms in naturally deformed peridotites. Earth Planet. Sci. Lett. 248 (1), 438–450. http://dx.doi.org/10.1016/j.epsl.2006.06.006.

Wassmann, S., Stöckhert, B., 2013. Rheology of the plate interface - Dissolution precipitation creep in high pressure metamorphic rocks. In: Tectonophysics, vol. 608, pp. 1–29. http://dx.doi.org/10.1016/j.tecto.2013.09.030.

Weiss, J.R., Qiu, Q., Barbot, S., Wright, T.J., Foster, J.H., Saunders, A., Brooks, B.A., Bevis, M., Kendrick, E., Ericksen, T.L., Avery, J., Smalley, R., Cimbaro, S.R., Lenzano, L.E., Barón, J., Báez, J.C., Echalar, A., 2019. Illuminating subduction zone rheological properties in the wake of a giant earthquake. Sci. Adv. 5 (12), eaax6720. http://dx.doi.org/10.1126/sciadv.aax6720.

Wenk, H.R., Yu, R., Cárdenes, V., Lopez-Sanchez, M.A., Sintubin, M., 2020. Fabric and anisotropy of slates: From classical studies to new results. J. Struct. Geol. 138, 104066. http://dx.doi.org/10.1016/J.JSG.2020.104066.

Wheeler, J., 1992. Importance of pressure solution and coble creep in the deformation of polymineralic rocks. J. Geophys. Res.: Solid Earth 97 (B4), 4579–4586. http://dx.doi.org/10.1029/91JB02476.

Whitney, D.L., Evans, B.W., 2010. Abbreviations for names of rock-forming minerals. Am. Miner. 95 (1), 185–187. http://dx.doi.org/10.2138/am.2010.3371.

Williams, R.T., Fagereng, A., 2022. The role of quartz cementation in the seismic cycle: A critical review. Rev. Geophys. 60 (1), e2021RG000768.

Wintsch, R.P., Wathen, B.A., McAleer, R.J., Walters, J., Matthews, J.A., 2024. Deformation by pressure solution and grain boundary sliding in a retrograde shear zone in Southern New England, USA. Am. J. Sci. 324, http://dx.doi.org/10.2475/001c.125064, URL https://ajsonline.org/article/125064-deformation-by-pressure-solution-and-grain-boundary-sliding-in-a-retrograde-shear-zone-in-southern-new-england-usa.

Wintsch, R.P., Yi, K., 2002. Dissolution and replacement creep: a significant deformation mechanism in mid-crustal rocks. J. Struct. Geol. 24 (6), 1179–1193. http://dx.doi.org/10.1016/S0191-8141(01)00100-6.

Woodcock, N., Mort, K., 2008. Classification of fault breccias and related fault rocks. Geol. Mag. 145 (3), 435–440. http://dx.doi.org/10.1017/S0016756808004883.

Yamasaki, T., Wright, T.J., Houseman, G.A., 2014. Weak ductile shear zone beneath a major strike-slip fault: Inferences from earthquake cycle model constrained by geodetic observations of the western North Anatolian Fault Zone. J. Geophys. Res. Solid Earth 119 (4), 3678–3699. http://dx.doi.org/10.1002/2013JB010347.

Yardley, B.W.D., 1983. Quartz veins and devolatilization during metamorphism. J. Geol. Soc. 140 (4), 657–663. http://dx.doi.org/10.1144/gsjgs.140.4.0657.

Zertani, S., Menegon, L., Pennacchioni, G., Buisman, I., Corfu, F., Jamtveit, B., 2023. Protracted localization of metamorphism and deformation in a heterogeneous lower-crustal shear zone. J. Struct. Geol. 176, 104960. http://dx.doi.org/10.1016/j.jsg.2023.104960.